RSC Advances

PAPER

View Article Online
View Journal | View Issue

Cite this: *RSC Adv.*, 2024, **14**, 32700

Theoretical investigations of optoelectronic properties, photocatalytic performance as a water splitting photocatalyst and band gap engineering with transition metals (TM = Fe and Co) of K_3VO_4, Na_3VO_4 and $Zn_3V_2O_8$: a first-principles study

Muhammad Awais Ali,[a] Maryam Noor Ul Ain,[a] Asim Mansha,*[a] Sadia Asim[b] and Ameer Fawad Zahoor *[a]

First-principles density functional investigations of the structural, electronic, optical and thermodynamic properties of K_3VO_4, Na_3VO_4 and $Zn_3V_2O_8$ were performed using generalized gradient approximation (GGA) *via* ultrasoft pseudopotential and density functional theory (DFT). Their electronic structure was analyzed with a focus on the nature of electronic states near band edges. The electronic band structure revealed that between 6% Fe and 6% Co, 6% Co significantly tuned the band gap with the emergence of new states at the gamma point. Notable variations were highlighted in the electronic properties of $Na_3V_{(1-x)}Fe_xO_4$, $Na_3V_{(1-x)}Co_xO_4$, $K_3V_{(1-x)}Fe_xO_4$, $K_3V_{(1-x)}Co_xO_4$, $Zn_{3(1-x)}V_{2(1-x)}Co_xO_8$ and $Zn_{3(1-x)}V_{2(1-x)}Fe_xO_8$ (where $x = 0.06$) due to the different natures of the unoccupied 3d states of Fe and Co. Density of states analysis as well as α (spin up) and β (spin down) magnetic moments showed that cobalt can reduce the band gap by positioning the valence band higher than O 2p orbitals and the conduction band lower than V 3d orbitals. Mulliken charge distribution revealed the presence of the $6s^2$ lone pair on Zn, greater population and short bond length in V–O bonds. Hence, the hardness and covalent character develops owing to the V–O bond. Elastic properties, including bulk modulus, shear modulus, Pugh ratio and Poisson ratio, were computed and showed $Zn_3V_2O_8$ to be mechanically more stable than Na_3VO_4 and K_3VO_4. Optimal values of optical properties, such as absorption, reflectivity, dielectric function, refractive index and loss functions, demonstrated $Zn_3V_2O_8$ as an efficient photocatalytic compound. The optimum trend within finite temperature ranges utilizing quasi-harmonic technique is illustrated by calculating thermodynamic parameters. Theoretical investigations presented here will open up a new line of exploration of the photocatalytic characteristics of orthovanadates.

Received 29th July 2024
Accepted 1st October 2024

DOI: 10.1039/d4ra05492j

rsc.li/rsc-advances

1. Introduction

Oxide-based semiconductors as water splitting photocatalysts have gained much attention in an effort to help with environmental preservation and the growing energy issue facing our society.[1] Owing to the world's extensive reliance on less efficient non-renewable fossil fuels (*e.g.*, coal, oil, and ethanol), a substantial amount of carbon dioxide is produced, which causes the greenhouse effect. One of the most promising alternatives to fossil fuels is the conversion of water into elemental components using incident photons. Because of its exceptionally clean combustion and green impact on the environment, photocatalytic materials furnish a direct pathway for converting solar radiation into hydrogen fuel.[2] A TiO_2 photocatalyst was firstly utilized for the efficient conversion of solar energy into chemical energy and emphasized the development of a photocatalytic system having the potential to split water into H_2 and O_2.[3,4] Unfortunately, its practical applications are limited by its fairly wide band gap as UV photons are the only primary source for its photocatalytic activity.[5] However, only 4% of solar energy is accessible. It is possible to develop photocatalytic materials that rely on less intense but more prevalent visible light that can harness a significant portion of the solar spectrum.[6] Such a compelling rationale for obtaining a stable, efficient, and cost-effective photocatalyst remains a goal to pursue for application in the field of photochemical cells (PECs).

The major role of a photocatalyst is to absorb incident light and create charge carriers, *i.e.*, electrons and holes. With the absorption of light having wavelengths equal to the band gap of the semiconductor, electrons are excited from the valence band

[a]*Department of Chemistry, Government College University Faisalabad, Pakistan. E-mail: asimmansha@gcuf.edu.pk; fawad.zahoor@gcuf.edu.pk*

[b]*Department of Chemistry, Government College Women University Faisalabad, Pakistan*

(VB) to the conduction band (CB), creating holes in the VB.[7] These charge carriers can then interact with pollutants, undergo oxidation–reduction processes, and result in products being adsorbed on the semiconductor's surface. The hole in the valence band and electrons in the conduction band can recombine at the same time. Effective light absorption, high redox potential, and limiting the photoinduced charge recombination are helpful methods of chemical conversion that improve the photocatalytic process efficiency.[8,9]

Recent studies on photosensitive materials for solar energy conversion have mainly focused on two primary goals: modification of conventional photocatalysts and development of a novel photocatalyst or photocatalytic system.[10] Moreover, due to their relative stability against photocorrosion (photo-oxidative disintegration), environmental friendliness, and ease of production, metal oxide semiconductors had attracted a lot of attention.[11] To date, the most efficient semiconductor photocatalysts to be reported are Fe_2O_3,[12] ZrO_2,[13] ZnO,[14] SnO_2,[15] TiO_2 (ref. 16) and bismuth halides.[17]

Vanadates have gained much attention due to their interesting physicochemical properties and exceptional performance.[18] They are preferred over titanium and zinc oxide photocatalysts due to their narrower band gap,[19] lower recombination rate,[20,21] and higher quantum efficiency.[22] Simultaneously, the complex structural chemistry of vanadates, which readily adapt to various shapes, including tetrahedral, distorted octahedral and dodecahedral, demonstrates their unique character. Due to the structural differences, they may be applied as photocatalysts or optoelectronic materials. The V-3d orbital usually offers a lower conduction band in the band gap structure, which is why vanadates are regarded as potent visible light-driven photocatalysts.[23] Having isolated discrete units, the orthovanadates (VO_4^{-3}) class is the simplest of all vanadates. Numerous visible-light activated photocatalysts, such as YVO_4,[24] $InVO_4$,[25] and $BiVO_4$,[26] have been reported for hydrogen production and the photodegradation of dyes.

This research work focuses on the systematic theoretical comparison of alkali-metal orthovanadate (K_3VO_4, Na_3VO_4) with transition metal orthovanadate ($Zn_3V_2O_8$). Having exceptional chemical strength, low band gap, economical, and an eco-friendly nature, one of the most promising photocatalysts for pollutant degradation and water splitting process is $Zn_3V_2O_8$. Sajid *et al.* reported that $Zn_3(VO_4)_2$ and its hydrates are effective photocatalysts and solar energy conversion materials.[27] Slobodin *et al.* proposed the color features and luminescence behavior of AVO_3 (A = K, Rb, and Cs), and reported on the synthesis of $M_3V_2O_8$ (M = Mg, Zn) by solid-state reaction method.[28]

Cobalt (Co) has been reported as an efficient dopant with a suitable valence band structure to photo-oxidize water to H_2, while having a band gap covering the entire range of visible light. Examples include the Co-doped Fe_2O_3–TiO_2,[29] Co^{2+}-doped-TiO_2,[30] $LaCo_xFe_{1-x}O_3$ (x = 0.01, 0.05, 0.1),[31] and $BiFe_{1-x}Co_xO_3$ (x = 0, 0.025, 0.05, 0.075 & 0.10).[32] In the same way, iron (Fe) has also been found as an effective dopant in various water splitting photocatalysts, such as Fe^{3+}-doped TiO_2,[33] Fe-doped TiO_2 and $SrTiO_3$ nanotubes,[34] Fe-doped $BiVO_4$,[35] and many others. Subsequent to the reported methodical photocatalytic efficiency of Fe and Co dopants, this research has also explored the enhancement of the photocatalytic efficiency with 6% Fe and 6% Co doped on Na_3VO_4, K_3VO_4 and $Zn_3V_2O_8$.

A review of the literature revealed that neither theoretical nor experimental studies of the electronic, elastic, optical, and thermodynamic parameters of these compounds have been reported yet. Herein, we report the first attempt to computationally design these water spitting photocatalysts with theoretical insights into the evolution of ($OH^{-\bullet}$) and $O_2^{-\bullet}$ radicals. The aforementioned motivation inspired us to carry out all these calculations using the full potential linear augmented plane wave (FPLAW) approach to ascertain the previous efforts on this subject, and offer reference data to experimentalists. Therefore, our investigation of all these parameters and band structure analysis with doping effects exhibited a reasonable explanation for the photocatalytic water splitting and degradation activity, which can assist in designing potentially effective vanadium-based photocatalyst materials.

2. Computational details

First-principles calculation of orthovanadates was accomplished through Cambridge Sequential Total Energy Package (CASTEP) code[36] in DS-BIOVIA Material Studio software.[37] Geometric optimization, electronic density of states, α (spin up) and β (spin down) magnetic moments, optical, elastic, and thermodynamic parameters have been computed using the FPLAPW density functional theory.[38] To study the exchange correlation interaction, the Perdew–Burke–Ernzerhof (PBE) function with generalized gradient approximation (GGA) scheme[39] was employed. Ultrasoft pseudopotentials were utilized to determine the valence electronic configuration (Na: $3s^1$, K $4s^1$, Zn: $3d^{10}4s^2$, V: $3d^34s^2$, and O: $2S^2$ $2P^4$). Convergence criteria were set to fine quality with kinetic energy, *i.e.*, 500 eV for Na_3VO_4, K_3VO_4 and 700 eV for $Zn_3V_2O_8$. Before performing electronic calculations, the lattice constants and atomic positions were fully optimized by keeping the residual force on each atom at less than 0.05 eV $Å^{-1}$. All geometry structures were fully relaxed with 0.002 Å force displacement and an energy value of 2×10^{-5} eV per atom. The Brillouin zone was sampled by the Monkhorst–Pack scheme with a mesh size of $8 \times 8 \times 6$ for Na_3VO_4, K_3VO_4, and $10 \times 5 \times 7$ for $Zn_3V_2O_8$. Meanwhile, a k-point grid of $1 \times 1 \times 1$ was used during the calculation of the elastic and thermodynamic properties of all models. The Mulliken population was computed to analyze the bond population and bonding nature. Moreover, the thermodynamic parameters were studied *via* Troullier–Martin norm-conserving pseudopotentials. The optical properties of the compounds were studied *via* frequency-dependent dielectric function $\alpha(\omega)$.[40]

$$\alpha(\omega) = \sqrt{2}\omega \left[\sqrt{\varepsilon_1{}^2(\omega) + \varepsilon_2{}^2(\omega)} - \varepsilon_1(\omega)\right]^{\frac{1}{2}}$$

3. Results and discussion

3.1. Crystal structure

The optimized structures of the orthorhombic ($Zn_3V_2O_8$) and tetragonal (Na_3VO_4 and K_3VO_4) phases are shown in Fig. 1a. The $Zn_3V_2O_8$ crystal was constructed in the *Cmca* space group, having three independent lattice parameters such as $a = 6.18$ Å, $b = 11.76$ Å, $c = 8.38$ Å. The crystal is composed of isolated VO_4 tetrahedra, spreading around the Zn atoms to form the ZnO_8 octahedra. The VO_4^{3-} tetrahedra share edges with the ZnO_8 dodecahedron, forming a chain parallel to the environment of the V-atoms.[41]

There are two independent lattice parameters, such as '*a*' and '*c*', for the tetragonal phase structure. The unit cell parameters are summarized in Table 1. There are two inequivalent coordinated sites in the Na_3VO_4 crystal system shown in Fig. 1b. In the first site, it forms a distorted tetrahedron (NaO_4) that gets bonded with four oxygen atoms, thereby sharing corners with the VO_4 tetrahedron. Secondly, Na coordinates with four oxygen atoms and forms NaO_4, which shares sites with the VO_4 and NaO_4 tetrahedra.[42] Similar to Na_3VO_4, the tetragonal crystal structure K_3VO_4 crystallizes with the $I\bar{4}2m$ space group, in which V ions are tetrahedrally coordinated. Meanwhile, K^{1+} ions have two types of chemically distinct environments, which are depicted in Fig. 1. In the first environment, K^{1+} is bonded to four oxygen atoms, forming a distorted trigonal pyramid that shares edges with the VO_4 tetrahedra. At the second site, the K^{1+} ions combine with four oxygen atoms to form the KO_4 tetrahedra.[19]

When foreign atoms are doped into the host lattice, the lattice distorts as a result of changes in the ionic radii and electronic states. However, the lattice distortions in the Co-doped and Fe-doped $Zn_3V_2O_8$, K_3VO_4, and Na_3VO_4 are not apparent after placing the dopant atom, which could be explained by the low impurity concentration and similar radii.

3.2. Band structure

To better characterize the electronic properties, the band structure provides significant information. Around the Fermi level, the electronic structures exhibit separation of the conduction and valence bands.[43] Here, the Fermi level is set to zero. A set of certain line segments linking distinctive Brillouin zone (BZ) points, as well as those connecting the distinctive BZ sites with the Γ-points, are chosen as the band pathways (Fig. 2). Fig. 3a, 4a and 5a illustrate the high symmetry points along the selected Brillouin zone path: $G(0\ 0\ 0) - Z(0\ 0\ 0.5) - T(-0.5\ 0\ 0.5)$

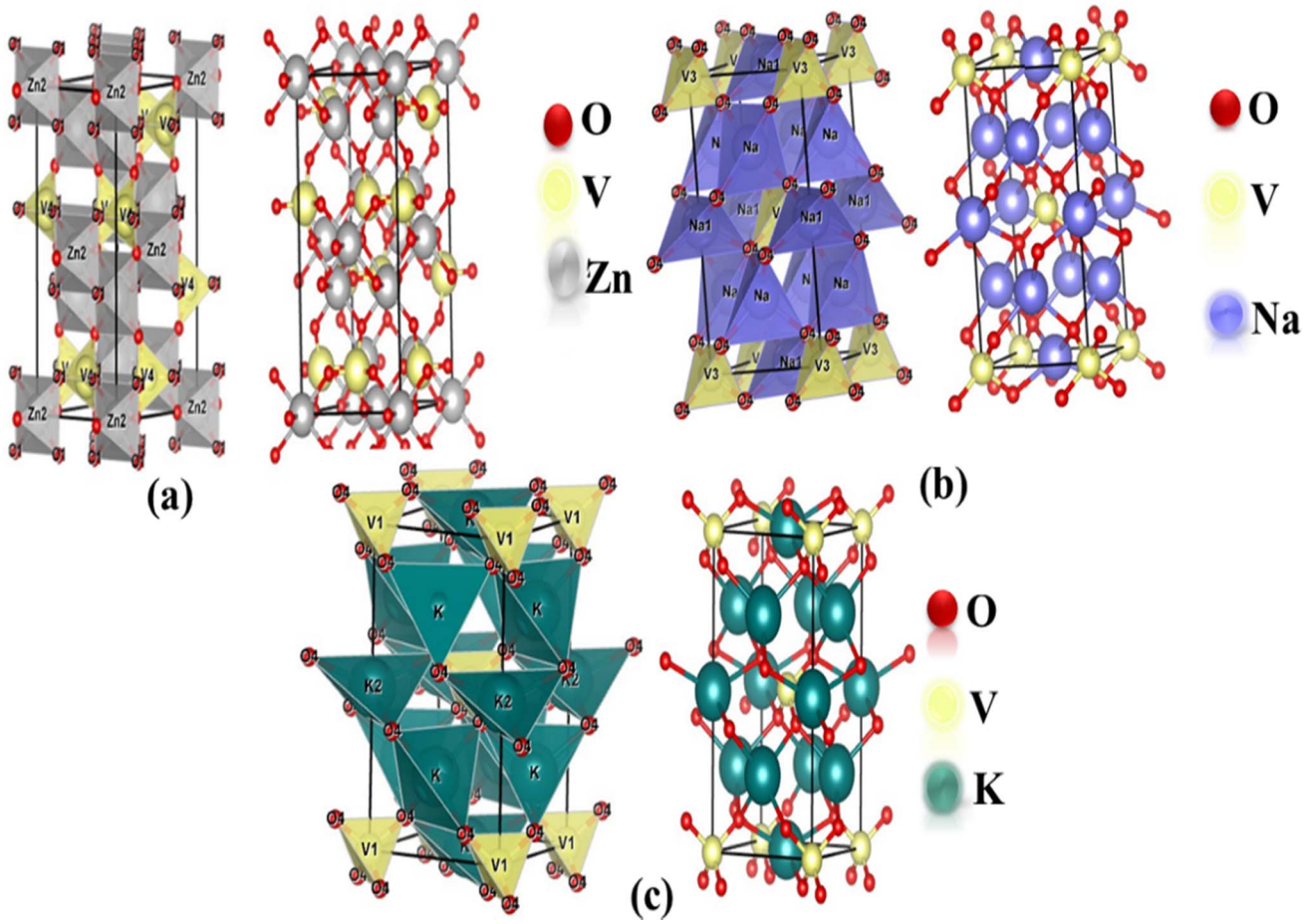

Fig. 1 Mixed polyhedral and ball-and-stick model of the optimized crystal structures of (a) $Zn_3V_2O_8$ (orthorhombic), (b) Na_3VO_4 (tetragonal) and (c) K_3VO_4 (tetragonal).

Table 1 Optimized lattice parameters, cell volume, angles and lattice energies of $Zn_3V_2O_8$, $Zn_{3(1-0.06)}V_{2(1-0.06)}Fe_{0.06}O_8$, $Zn_{3(1-0.06)}V_{2(1-0.06)}Co_{0.06}O_8$, Na_3VO_4, $Na_3V_{(1-0.06)}Fe_{0.06}O_4$, $Na_3V_{(1-0.06)}Co_{0.06}O_4$, K_3VO_4, $K_3V_{(1-0.06)}Fe_{0.06}O_4$, and $K_3V_{(1-0.06)}Co_{0.06}O_4$

	Lattice constants			Angles				
Crystals	a (Å)	b (Å)	c (Å)	α	β	γ	Cell volume $(Å)^3$	Lattice energy (eV)
$Zn_3V_2O_8$	6.15	11.70	8.34	90	90	90	600.87	−50340.43
$Zn_{3(1-0.06)}V_{2(1-0.06)}Fe_{0.06}O_8$	6.25	11.87	8.13	90	90	90	603.62	−52422.60
$Zn_{3(1-0.06)}V_{2(1-0.06)}Co_{0.06}O_8$	6.20	11.76	8.36	90	90	90	609.85	−52831.13
Na_3VO_4	5.02	5.02	9.79	90	90	90	247.01	−15288.88
$Na_3V_{(1-0.06)}Fe_{0.06}O_4$	5.06	5.06	9.78	90	90	90	250.42	−15072.91
$Na_3V_{(1-0.06)}Co_{0.06}O_4$	5.09	5.09	9.80	90	90	90	254.42	−15134.94
K_3VO_4	5.72	5.72	10.05	90	90	90	329.38	−12140.37
$K_3V_{(1-0.06)}Fe_{0.06}O_4$	5.8	5.8	10	90	90	90	338.68	−11985.15
$K_3V_{(1-0.06)}Co_{0.06}O_4$	5.95	5.95	9.31	90	90	90	329.59	−11994.68

$Y(-0.5\ 0\ 0) - S(-0.5\ 0.5\ 0) - X(0\ 0.5\ 0) - U(0\ 0.5\ 0.5) - R(-0.5\ 0.5\ 0.5)$, $Z(0\ 0\ 0.5) - A(0.5\ 0.5\ 0.5) - M(0.5\ 0.5\ 0.0) - G(0\ 0\ 0) - Z(0\ 0\ 0.5) - R(0\ 0.5\ 0.5) - X(0\ 0.5\ 0) - G(0\ 0\ 0)$, and $Z(0\ 0\ 0.5) - A(0.5\ 0.5\ 0.5) - M(0.5\ 0.5\ 0) - G(0\ 0\ 0) - Z(0\ 0\ 0.5) - R(0\ 0.5\ 0.5) - X(0\ 0.5\ 0.0) - G(0\ 0\ 0)$ for $Zn_3V_2O_8$,[44] Na_3VO_4 (ref. 45) and K_3VO_4 (ref. 46) photocatalysts, respectively. From Fig. 3a and 4a, the top of the valence band is ostensibly obtained within the G line for $Zn_3V_2O_8$ and at the M line for Na_3VO_4. Subsequently, the bottom of the conduction band is connected in the Y point and G point between the SIG of the Brillouin zone for $Zn_3V_2O_8$ and Na_3VO_4; hence, indicating the indirect band gap. In the case of K_3VO_4, the G point specifies the direct band gap between the valence and conduction bands, as shown in Fig. 5a. Concerning the photocatalytic activity, the indirect band gap is more effective than direct ones.[47] Due to the difference in the momentum between the location of the two high symmetry points, it prevents the recombination of excited electrons with holes.[48] The estimated theoretical band gaps of $Zn_3V_2O_8$, Na_3VO_4 and K_3VO_4 are 2.69 eV, 3.80 eV and 3.65 eV, respectively.[49] The electronic properties of zinc orthovanadate are in good agreement with the reported theoretical study of orthovanadates.[50]

The band gap varies inversely with the atomic mass. This agrees with the sequence of band gap values for the selected compounds, such as Na_3VO_4 > K_3VO_4 > $Zn_3V_2O_8$.[51] However, among all compounds, the dramatic decrease in the band gap of $Zn_3V_2O_8$ is due to the transition metal involving the d-orbital in bonding. Specifically, Zn (3d-orbital) is involved in the excitation of electrons from VB to CB.[19]

3.3. Doping/band gap engineering

To construct the band gap covering the whole range of visible light, 6% Fe was doped on the vanadium atom of Na_3VO_4 and K_3VO_4. Similarly, 6% Co was doped on the V-3D sites of the crystal lattices, and their band structures were compared. Meanwhile, in the case of $Zn_3V_2O_8$, the doping of 6% Fe or Co only on the V-3D sites was not significant. However, doping both Zn and V atoms with 6% Fe or Co magnified the narrowing of the band gap. The Co-doped $Zn_3V_2O_8$ system shows the narrowest energy gap between the dopant states and the VBM. Fig. 3 shows the reduction in the band gap values as follows: 2.69 eV > 1.72 eV > 1.68 eV for $Zn_3V_2O_8$ > $Zn_{3(1-0.06)}V_{2(1-0.06)}Fe_{0.06}O_8$ > $Zn_{3(1-0.06)}V_{2(1-0.06)}Co_{0.06}O_8$, respectively. Meanwhile, in the case of Na_3VO_4, $Na_3V_{(1-0.06)}Fe_{0.06}O_4$ and $Na_3V_{(1-0.06)}Co_{0.06}O_4$, the computed band gaps are 3.80 eV, 2.99 eV and 2.59 eV, respectively (Fig. 4). Similarly, the sequence of reduction in the band gap has been observed as 3.68 eV > 2.76 eV > 2.58 eV for K_3VO_4 > $K_3V_{(1-0.06)}Fe_{0.06}O_4$ > $K_3V_{(1-0.06)}Co_{0.06}O_4$, respectively (Fig. 5). In all three host crystal lattices, cobalt is computed as being a vital dopant for enhancing their photocatalytic activity.

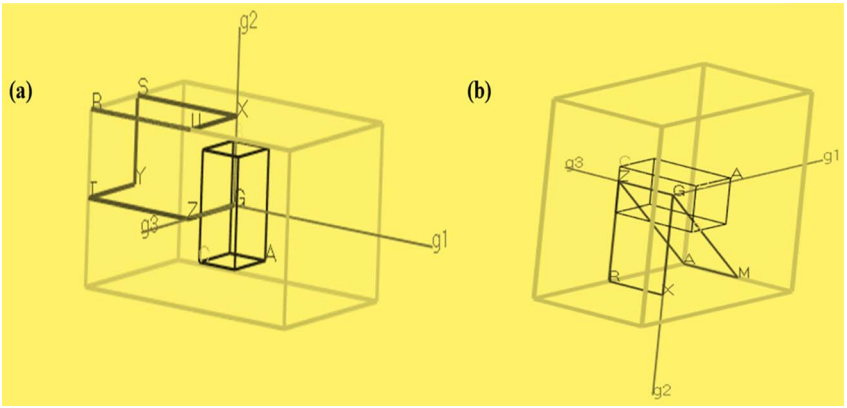

Fig. 2 Brillouin zone showing k points of (a) orthorhombic $Zn_3V_2O_8$ as well as (b) tetragonal Na_3VO_4 and K_3VO_4.

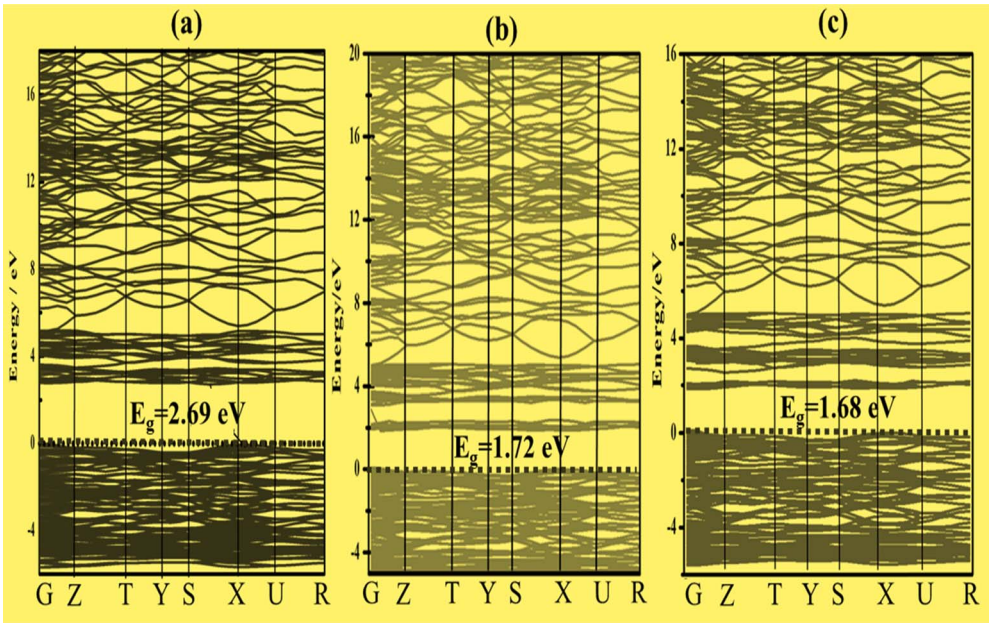

Fig. 3 Band structure with the indicated dashed line at 0 eV as the Fermi level of (a) $Zn_3V_2O_8$, (b) $Zn_{3(1-0.06)}V_{2(1-0.06)}Fe_{0.06}O_8$ and (c) $Zn_{3(1-0.06)}V_{2(1-0.06)}Co_{0.06}O_8$.

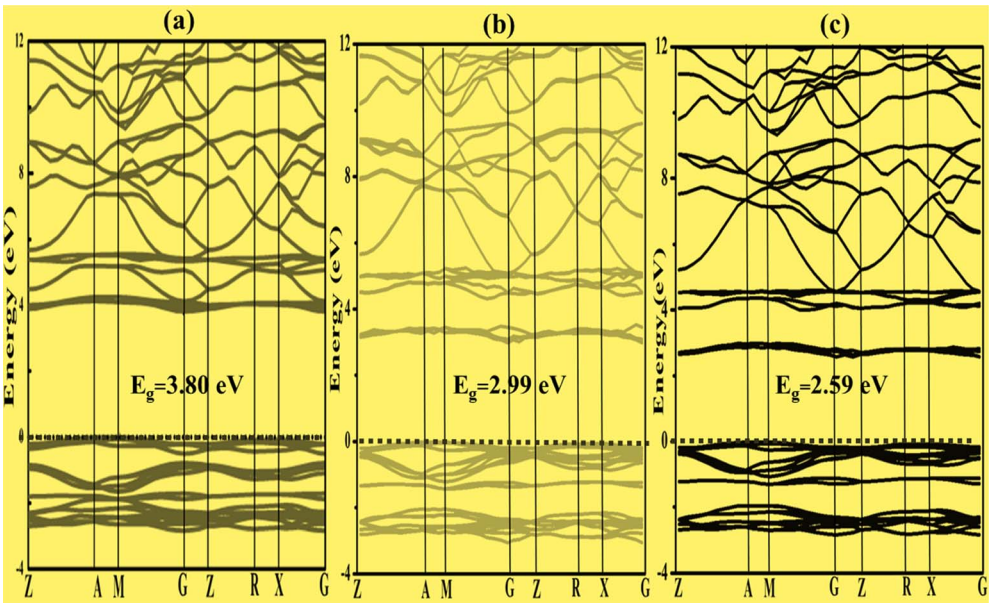

Fig. 4 Band structure of (a) Na_3VO_4, (b) $Na_3V_{(1-0.06)}Fe_{0.06}O_4$, and (c) $Na_3V_{(1-0.06)}Co_{0.06}O_4$, in which the Fermi level is referenced as 0 eV as indicated by the horizontal dashed line.

3.4. Density of state

To develop qualitative insight into the nature of orbitals and their splitting, the total and projected density of states are examined. This provided substantial information for the characterization of the electronic properties of the materials. As a central atom, vanadium has a 3-d orbital that splits into two sets. The "e" state (including $3d_{x^2y^2}$ and $3d_{z^2}$) and t_2 state (having $3d_{xy}$, $3d_{yz}$, and $3d_{xz}$) are considered as two distinct parts in crystal field theory.[52] The conduction band is mainly composed of the vanadium 3d atom for tetragonal and orthorhombic phase structures. This band falls in the energy region between 0 and 10 eV. There is also a minor contribution of O-2p states, resulting in p–d hybridization.[53]

The upper valence band of $Zn_3V_2O_8$ ranging from 0–3.5 eV is mainly dominated by the O-2p state, which is the major hallmark of oxide-based semiconductor materials, as shown in Fig. 6. The V-3d and Zn-3d orbitals are also involved in the

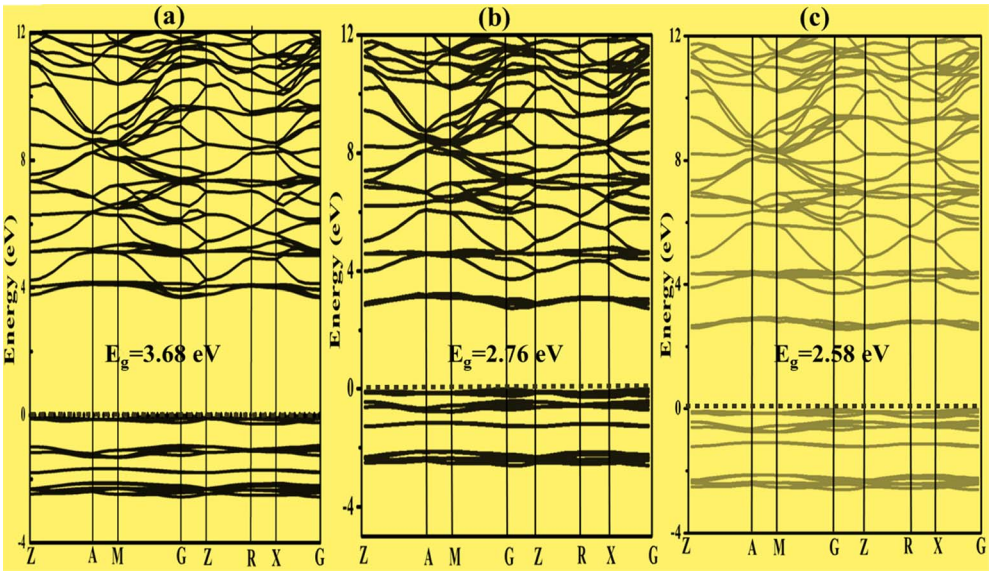

Fig. 5 Band structure of (a) K_3VO_4, (b) $K_3V_{(1-0.06)}Fe_{0.06}O_4$ and (c) $K_3V_{(1-0.06)}Co_{0.06}O_4$, in which the Fermi level is referenced as 0 eV as indicated by the horizontal dashed line.

upper valence band. One of the most striking attributes is the involvement of Zn-3d in the entire VB. However, p–d hybridization results in a strong covalent interaction between the Zn-3d and O-2p states.[50] The calculated DOS and PDOS for the Fe-doped and Co-doped systems with 6% concentration are compared in Fig. 7a and b. The Fermi level of each doped system lies within the dopant states, which means that both dopants inherently have empty states that can accept the active electrons. The dopant states become eminently closer in the case of the Co-dopant, and the energy gap is noted to be significantly narrower for $Zn_{3(1-0.06)}V_{2(1-0.06)}Co_{0.06}O_8$. Moreover, expansion of the VBM can be attributed to the increasing contribution of Co-3d states in the conduction band, as evident from the PDOS plots shown in Fig. 6b. Similarly, Fig. 7a and

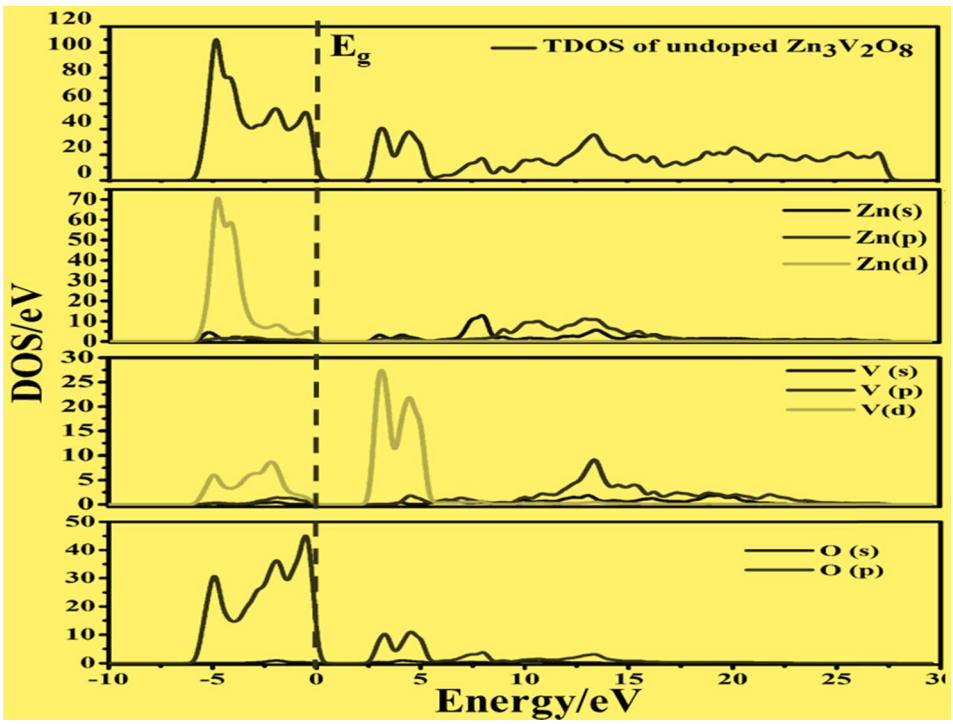

Fig. 6 Calculated total density of states and partial density of states of pure $Zn_3V_2O_8$ showing the O-2p states and V-3d states below and above the Fermi level (E_g).

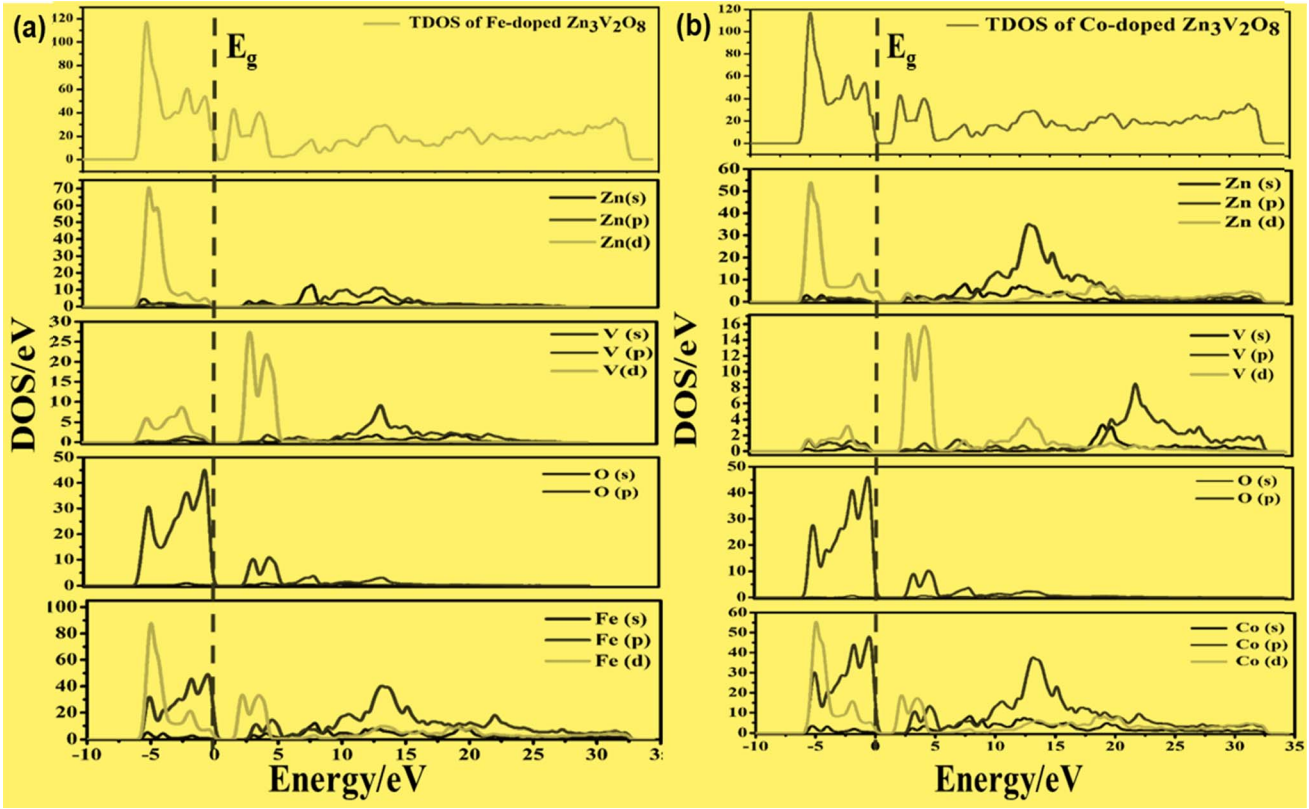

Fig. 7 Calculated total density of states and partial density of states of (a) $Zn_{3(1-0.06)}V_{2(1-0.06)}Fe_{0.6}O_8$ and (b) $Zn_{3(1-0.06)}V_{2(1-0.06)}Co_{0.06}O_8$, showing the O-2p, Fe-3p and Co-3p states in VBM, along with the V-3d, Fe-3d and Co-3d states in CBM.

b show that the contribution and distribution of O-2p states in the valence bands are not significantly altered.

On the other hand, the VBM of the tetragonal phase system is composed of O 2p states. There is a contribution of V 3d, Na 3s, and K 4s in the CBM of these isostructural crystal systems, as shown in Fig. 8 and 10. Fig. 9a and 11a reveal that the Fe-dopant prominently induces its 3d before the V 3d state in $Na_3V_{(1-0.06)}Fe_{0.06}O_4$ and $K_3V_{(1-0.06)}Fe_{0.06}O_4$, thus placing the CBM near the Fermi level (E_g). Meanwhile, in the case of the Co-doped alkali metal orthovanadates, such as $Na_3V_{(1-0.06)}Co_{0.06}O_4$ and $K_3V_{(1-0.06)}Co_{0.06}O_4$, the CBM has been computed to shift closer to E_g, resulting in the vital reduction of the band gap due to the low-lying Co 3d state (Fig. 9a and b).

3.5. Magnetic properties

Since Fe and Co are magnetic elements[54] as compared to V, the inversion symmetry of the atomic geometry diminishes in the direction normal to the plane of symmetry, while it still persists within the plane. Nevertheless, it is possible for spin polarization to break the in-plane inversion symmetry of spin-resolved electronic states, resulting in energetic spin splitting at the Fermi level.[55] Therefore, the spin electron density in real space and the spin-dependent orbital-resolved (partial) atomic-projected density of states (DOS) were calculated by collinear spin polarization to investigate the spin asymmetry magnetic order and the atom-orbital contributions to the spin magnetic moment.

In the total electron density, the major α (spin up) and β (spin down) components of the spin-polarized electrons are appreciably distinguished by the positive and negative spin densities of the s, p and d orbitals.[56] The α and β spin states for the undoped and doped $Zn_3V_2O_8$ Na_3VO_4 and K_3VO_4 are shown in Fig. 12–14, respectively. In $Zn_3V_2O_8$, the valence band is attributed mainly to the α-spin states of O 2p with a minor contribution from the 3d α-spin electrons of Zn and V. Particularly, the higher absolute value of the α-dominated spin density of the V-3d electrons in the conduction band compared to that of the β-dominated electrons indicates the presence of more α electrons than β electrons, as manifested in Fig. 12a. However, the α-spin magnetic moment predominantly originates in the conduction band from the spin-polarized components of the V-3d and Co-3d orbitals in $Zn_{2.82}V_{1.88}Co_{0.12}O_4$, and the V-3d and Fe-3d orbitals in $Zn_{2.82}V_{1.88}Fe_{0.12}O_4$ with an energetic-preferential spin splitting near the Fermi level, as shown in Fig. 12b and c.

For Na_3VO_4 and K_3VO_4, the entire crystal lattice comprises the α-dominated spin states of O-2p and V-3d near the Fermi level (Fig. 13 and 14). The valence band maximum (VBM) and conduction band minimum (CBM) are mainly from the α-spin states of the O-2p and V-3d orbitals. Meanwhile, the 3d α-spin states of the Fe and Co dopants significantly shifted the CBM close to the Fermi level. However, the β-dominated electrons occur less frequently in VBM and CBM (Fig. 13b, c and 14b, c). It is evident from the spin polarization that Co and Fe are

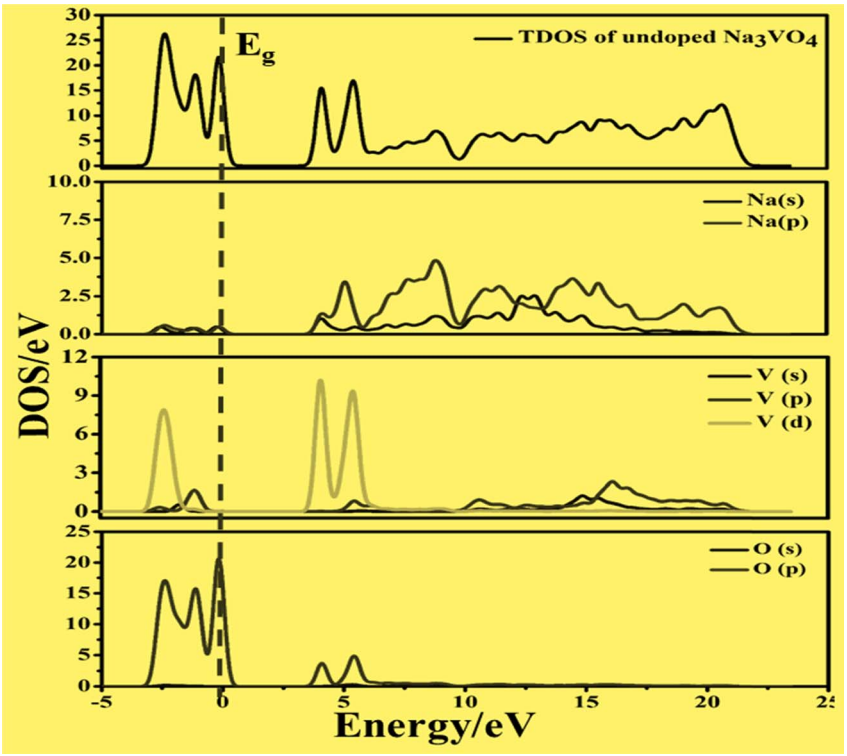

Fig. 8 Calculated total density of states (TDOS) and partial density of states of pure Na_3VO_4, showing O-2p and V-3d states below and above the Fermi level (E_g).

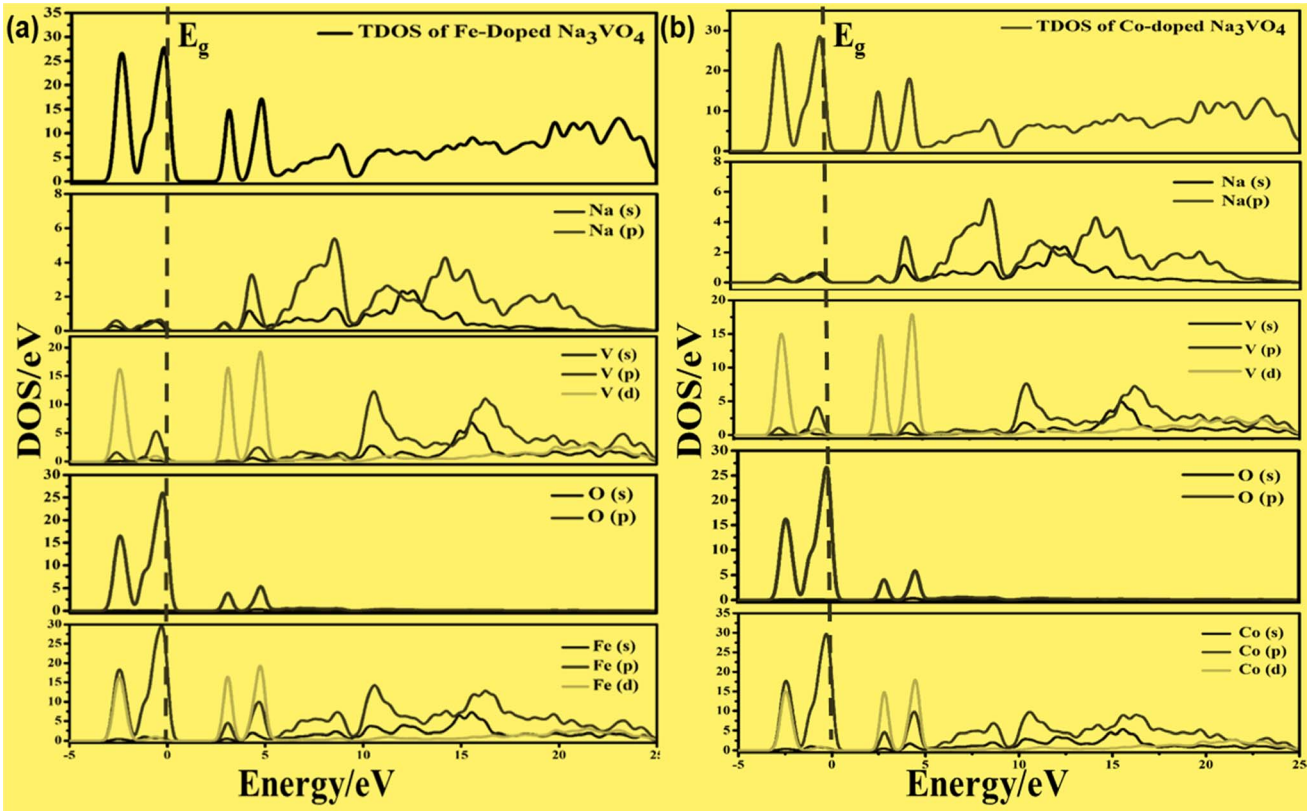

Fig. 9 Calculated total density of states (TDOS) and partial density of states of (a) $Na_3V_{(1-0.06)}Fe_{0.06}O_4$ and (b) $Na_3V_{(1-0.06)}Co_{0.06}O_4$, showing the O-2p, Fe-3p and Co-3p states in VBM, along with the V-3d, Fe-3d and Co-3d states in CBM.

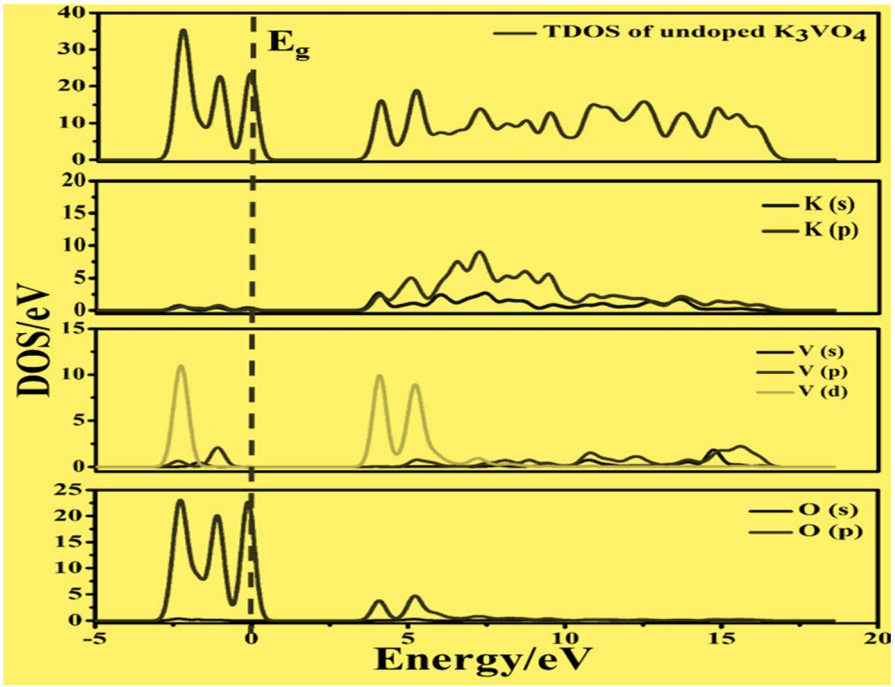

Fig. 10 Calculated total density of states (TDOS) and partial density of states of pure K_3VO_4, showing the O-2p states and V-3d states below and above the Fermi level (E_g).

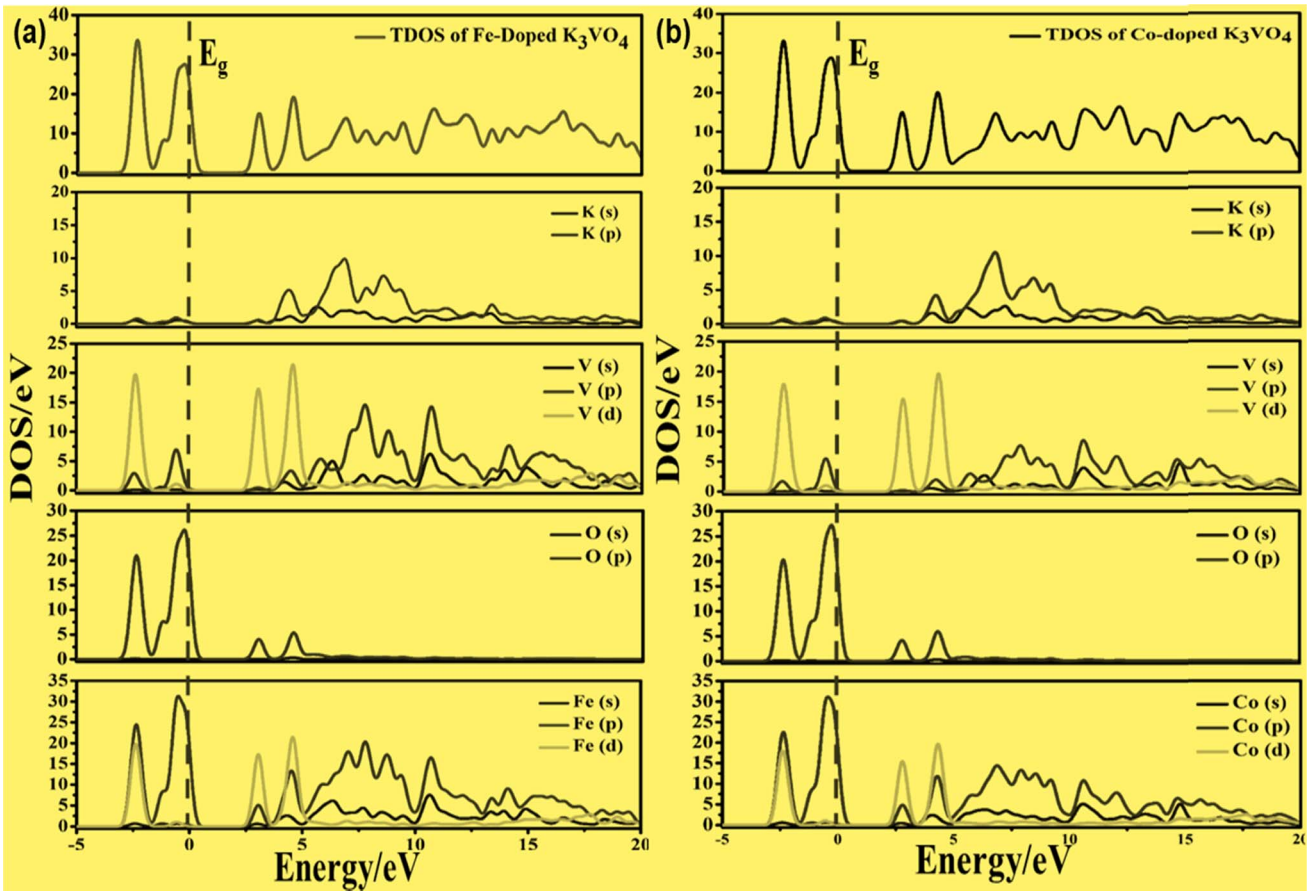

Fig. 11 Calculated total density of states (TDOS) and partial density of states of (a) $K_3V_{(1-0.06)}Fe_{0.06}O_4$ and (b) $K_3V_{(1-0.06)}Co_{0.06}O_4$, showing the O-2p, Fe-3p and Co-3p states in VBM, along with the V-3d, Fe-3d and Co-3d states in CBM.

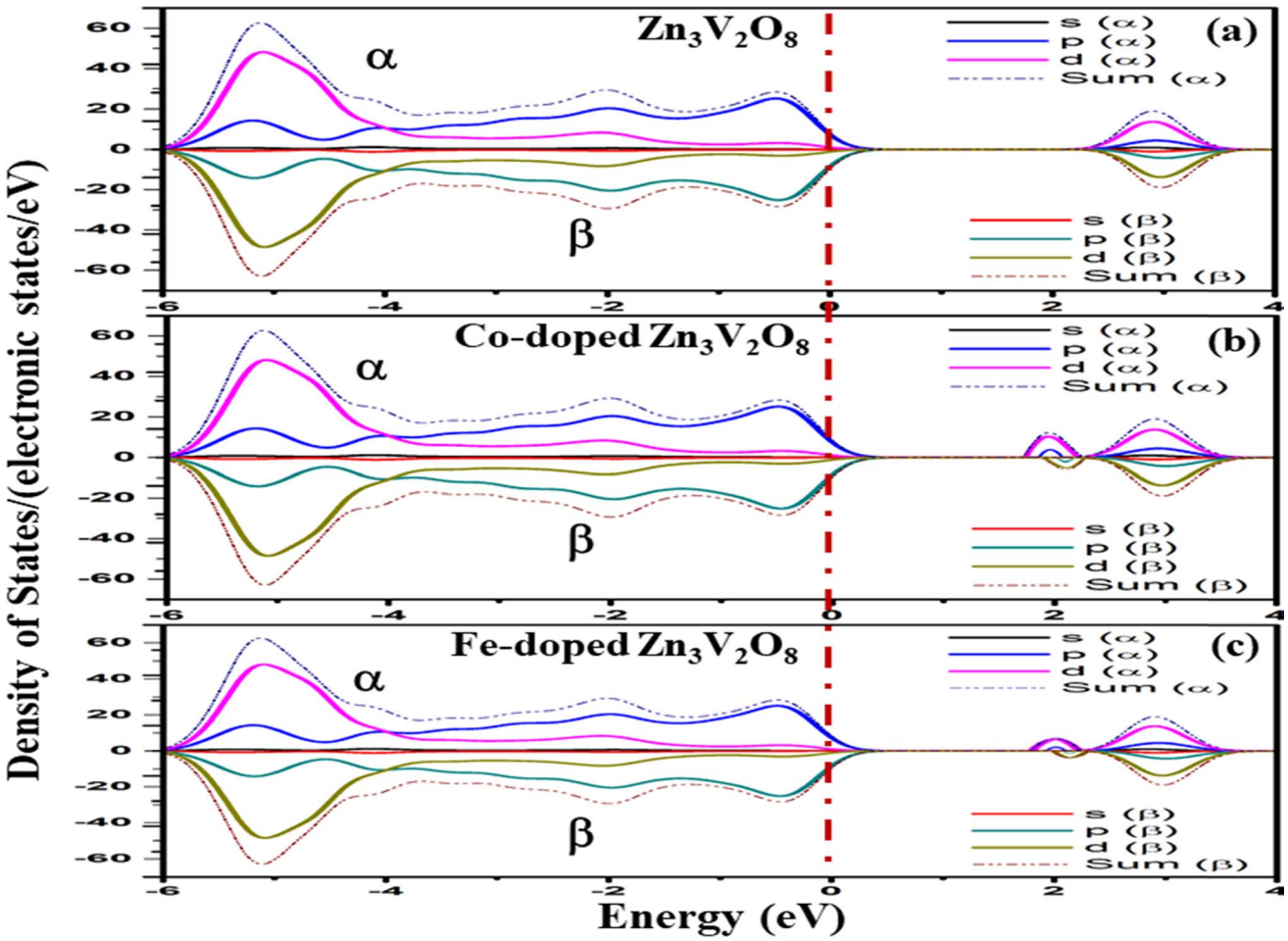

Fig. 12 Spin-up (↑) and spin-down (↓) partial density of states of (a) $Zn_3V_2O_8$, (b) $Zn_{3(1-0.06)}V_{2(1-0.06)}Co_{0.06}O_8$, and (c) $Zn_{3(1-0.06)}V_{2(1-0.06)}$-$Fe_{0.06}O_8$ with indicated dashed lines as the Fermi level (E_g).

magnetic metals because both up-spin and down-spin DOS cross the Fermi level with a clear polarization between the DOS of the two spin channels.[57] In $Zn_3V_2O_8$, Fe and Co established the p-type extrinsic semiconductor with the shifting of the Fermi level towards VB.[58] Meanwhile, in the case of Na_3VO_4 and K_3VO_4, DOS more prominently crosses the Fermi level, indicating Fe-doped and Co-doped p-type extrinsic semiconductors.

3.6. Mulliken population analysis

Mulliken charge analysis and bond population facilitated the investigation of the bonding behavior of the $Zn_3V_2O_8$, Na_3VO_4 and K_3VO_4 crystal systems. The bond population and atomic bond lengths are expressed in Table 2.

The R and V atoms of the photocatalytic systems have higher positive charge, while oxygen has a negative charge. The data sets in Table 3 demonstrate that charge transfer is carried out from R and V to O atoms. Moreover, the higher positive charge transfer values demonstrated the greater overlap between the atoms of the bonding atoms.[44]

The characteristic of a bond as either covalent or ionic can be evaluated by the overlap population of the orbitals. A complete ionic bond has a value of zero in the overlap bond population. Conversely, bonds having values greater than zero have a higher covalent character.[59] So, the stronger covalency is implied by the greater bond population, whereas the opposite is true for the ionic character. The V–O bond populations for these three systems (0.76, 0.74, 0.64, 0.67) are much higher than the R–O bonds (0.04, −0.05, 0.10, 0.08, 0.33, 0.20, 0.17). As compared to the R–O bond, the covalent character is stronger in the V–O bond. Na_3VO_4 and $Zn_3V_2O_8$ exhibit more covalent character, as listed in Table 2. Meanwhile, the bonding of K_3VO_4 is actually a mixture of covalent–ionic properties. Having greater bond population and shorter bond lengths, the V–O bonds also have a considerable impact on the hardness, instead of the R–O bonds, in the R_3VO_4 and $R_3V_2O_8$ crystal systems.

The crystal structures and electronic band structures have led to the conclusion that vanadium atoms develop covalent and ionic interactions with O to produce VO_4^{3+}, which confirmed the lack of a lone pair electron in the V atoms. Therefore, the interaction forces between R^{2+} and V^{5+} are directly related to the V–O bonds. The distortion in the Zn–O bond lengths in $Zn_3V_2O_8$ is due to the $4s^2$ or $6s^2$ lone pair of the transition metal (Zn^{+2}). The strong photocatalytic activity of visible light is greatly influenced by this attribute,[44] which seems favorable for $Zn_3V_2O_8$.

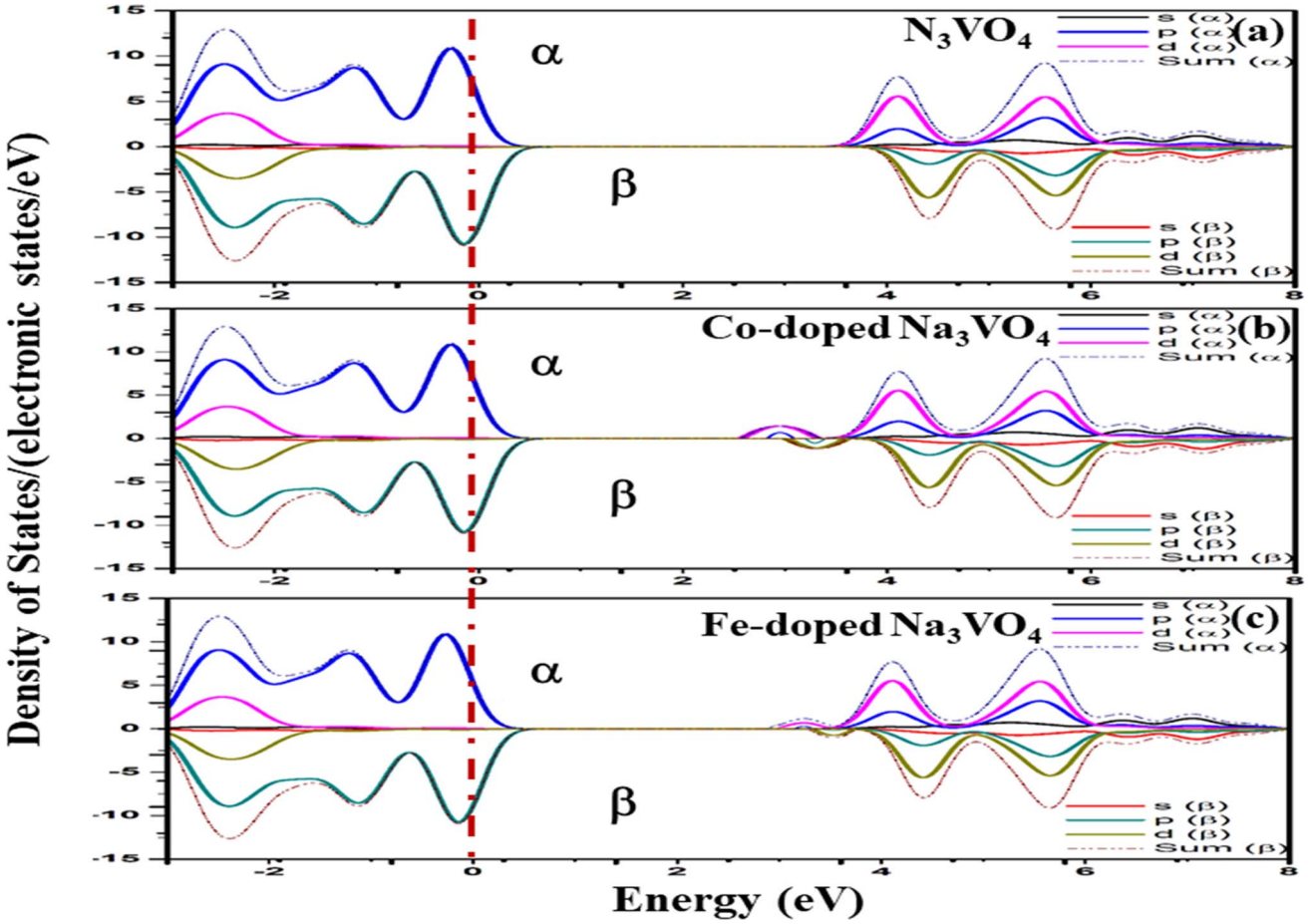

Fig. 13 Spin-up (↑) and spin-down (↓) partial density of states of (a) Na_3VO_4, (b)- $Na_3V_{(1-0.06)}Co_{0.06}O_4$, and (c) $Na_3V_{(1-0.06)}Fe_{0.06}O_4$ with indicated dashed lines as the Fermi level (E_g).

3.7. Elastic and mechanical properties

The Debye temperature, dynamic properties, and stress strain behavior are all influenced by a solid's mechanical properties and elastic constants, which are crucial parameters. Moreover, the structural stability and binding energy are associated with the elastic properties. As the elastic constants vary depending on the crystal symmetry,[60] there are six distinct elastic constants for the tetragonal systems: C_{11}, C_{33}, C_{44}, C_{66}, C_{12}, C_{13}.[61] Meanwhile, the orthorhombic system has nine independent elastic parameters; namely, C_{11}, C_{22}, C_{33}, C_{44}, C_{55}, C_{66}, C_{12}, C_{13}, C_{23}.[62] The positively defined quadratic form of the energy density, in which the coefficients are determined from the DFT calculations (elastic stiffness), fulfill the following fundamental criteria of the tetragonal and orthorhombic structures that explore the mechanical stability of the compounds.[63]

• Born stability standard for the tetragonal system (Na_3VO_4 and K_3VO_4):

$$C_{11} > |C_{12}|;\ 2C_{13}^2 < C_{33}\ (C_{11} + C_{12}),\ C_{44} > 0;\ C_{66} > 0$$

• Criteria for the mechanical stability of the orthorhombic system ($Zn_3V_2O_8$) is:

$$(C_{11} > 0;\ C_{11}C_{12} > C_{12}^2$$

$$C_{11}C_{22}C_{33} + 2C_{12}C_{13}C_{23} - C_{11}C_{23}^2 - C_{22}C_{13}^2 - C_{33}C_{12}^2 > 0$$

$$C_{44} > 0;\ C_{55} > 0;\ C_{66} > 0$$

Table 4 shows that the values of all elastic parameters are positive, and meet all aforementioned requirements. So, the crystal systems are mechanically stable.

To assess the aggregate average elastic characteristics of the crystal structure, additional approximations named as isostress (Reuss state) and isostrain (Voigt state) were used. Hill demonstrated that the Voigt and Reuss approximations accurately exhibit the upper and lower limits of the elastic constants. The Voigt (B_v) and Reuss (B_R) bulk modulus is given as:[64]

For the tetragonal system, the bulk modulus can be calculated as:[65]

$$B_v = \frac{(2(C_{11} + C_{12}) + C_{33} + 4C_{13})}{9}$$

$$B_R = \frac{C^2}{M}$$

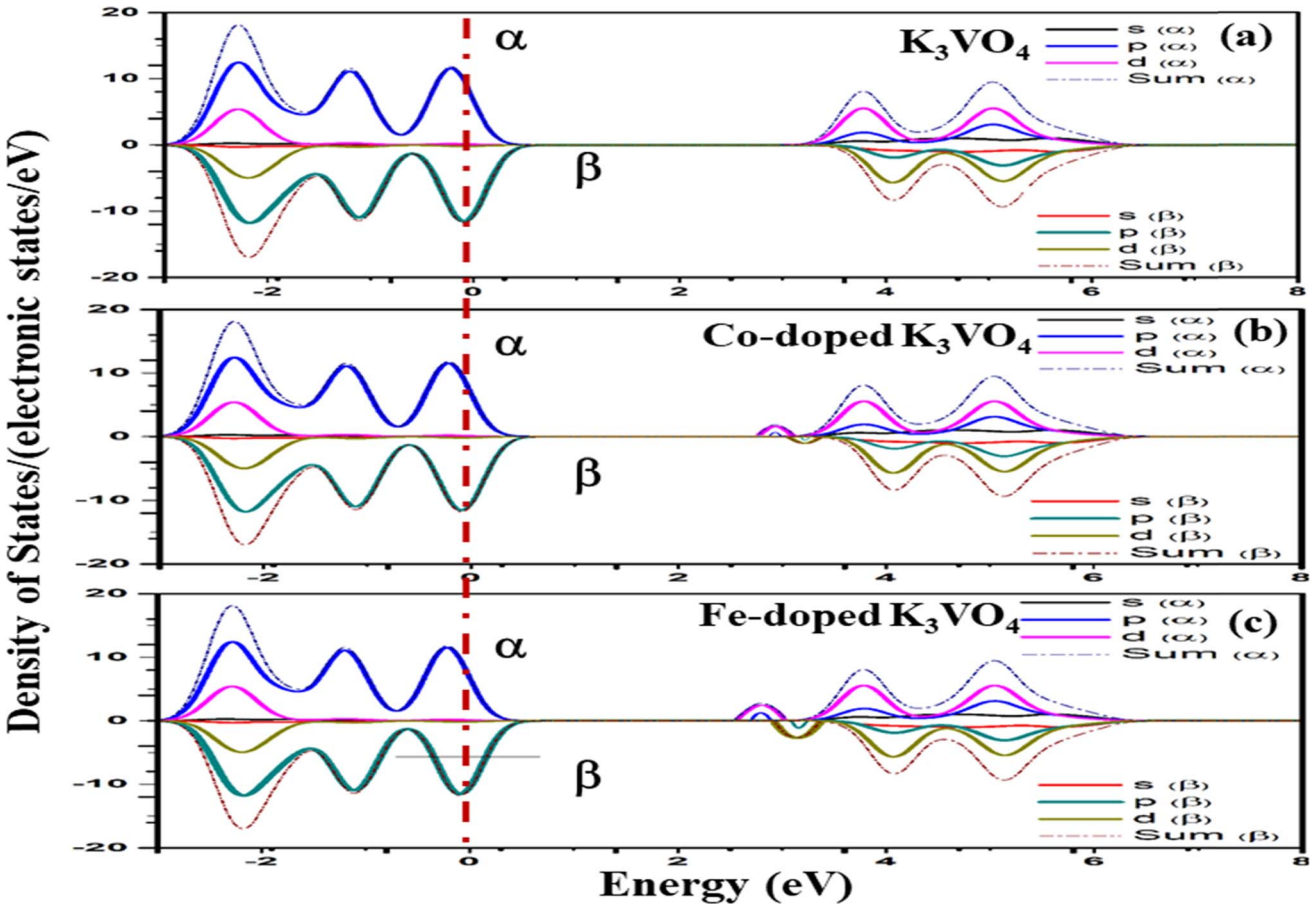

Fig. 14 Spin-up (↑) and spin-down (↓) partial density of states of (a) K_3VO_4, (b) $K_3V_{(1-0.06)}Co_{0.06}O_4$, and (c) $K_3V_{(1-0.06)}Fe_{0.06}O_4$ with indicated dashed lines as the Fermi level (E_g).

Table 2 Calculated bond lengths (Å) and bond populations of the $Zn_3V_2O_8$, Na_3VO_4 and K_3VO_4 crystal systems

Compounds	Population R–O	Bond length R–O/Å	Bond length V–O/Å	Population V–O
$Zn_3V_2O_8$	0.33, 0.20, 0.17	2.04, 2.23, 2.18	1.71, 1.74, 1.81	0.76, 0.67, 0.64
Na_3VO_4	0.10, 0.08	2.32, 2.36	1.73	0.74
K_3VO_4	0.04, −0.05	2.60, 2.8	1.74	0.76

whereas, $C^2 = (C_{11} + C_{12})\,C_{33} - 2{C_{13}}^2$, $M = C_{11} + C_{12} + 2C_{33} - 4C_{13}$

The Voigt–Reuss shear modulus is then derived as:

$$G_V = \frac{(M + 3C_{11} - 3C_{12} + 12C_{44} + 6C_{66})}{30}$$

$$G_R = \frac{15}{\left[\frac{(18B_V)}{C^2} + \frac{6}{(C_{11} - C_{12})} + \frac{6}{C_{44}} + \frac{3}{C_{66}}\right]}$$

The VRH averages for the shear modulus (G) and bulk modulus (B) are given as:

$$G_H = \frac{G_V + G_R}{2}, B_H = \frac{B_V + B_R}{2}$$

While the Young's modulus (E) and Poisson ratio (ν) are computed as:

$$E = \frac{9BG}{3B + G},\ \nu = \frac{3B - 2G}{2(3B + G)}$$

The bulk and shear modulus for the orthorhombic system can be calculated by the following equations:[66]

$$B_V = \frac{1}{9}(C_{11} + C_{22} + C_{33} + 2C_{12} + 2C_{13} + 2C_{23})$$

$$G_V = \frac{1}{15}(C_{11} - C_{12} - C_{13} + C_{22} - C_{23} + C_{33} + 3C_{44} + 3C_{55} + 3C_{66})$$

$$G_R = 15\left(\frac{4[C_{11}(C_{22}+C_{33}+C_{23})+C_{22}(C_{33}+C_{13}+C_{33}C_{12})-C_{12}(C_{23}+C_{12})C_{13}(C_{12}+C_{13})-C_{23}(C_{13}+C_{23})]}{\chi}+3\{(C_{44}^{-1}+C_{55}^{-1}+C_{66}^{-1})\}^{-1}\right)^{-1}$$

$$B_R = \chi(C_{11}(C_{22}+C_{33}-2C_{33})+C_{22}(C_{33}-2C_{13})-2C_{33}C_{12}+C_{12}(2C_{23}-C_{12})+C_{13}(2C_{12}-C_{13})+C_{23}(2C_{13}-C_{23}))^{-1}$$

$$G_H = \frac{G_V + G_R}{2}, B_H = \frac{B_V + B_R}{2}$$

The way to calculate the Young's modulus and Poisson ratio is the same as stated for the tetragonal systems. The Voigt and Reuss equations define the upper and lower limits of polycrystalline elastic constants, respectively, and the arithmetic mean of these two limits is used to estimate the realistic bulk and shear modulus. The bulk modulus (B) measures the resistance to volume change, along with the bond length caused by applied pressure. The significant strength of the solid bonds is an indication of the higher bulk modulus.[67] The condition of the bulk modulus stated as $C_{12} < B < C_{11}$ seems to satisfy all these crystal systems.

Panda & Chandran[68] developed equations to investigate the Young's modulus and Poisson ratio. The resistance to reversible deformation under shear stress was investigated by the shear modulus (G), which is known as the stiffness of a material. A greater shear modulus suggests a stronger degree of bonding between atoms.[69] As a result, the $Zn_3V_2O_8$ system is stiffer and exhibits stronger bonding than the other two systems.

Pugh's ratio defines the nature of bonding, which is either ionic or covalent, on the basis of the ductile and brittle character of the fabricated material. G/B < 6 indicates the ductility (ionic bonding) of the material, and the reverse is for the brittle (covalent bonding) nature.[70] Therefore, K_3VO_4 and $Zn_3V_2O_8$ have higher ductile nature.

The directionality of the covalent bonds is quantified by the Poisson ratio. In contrast to ionic materials, which have a Poisson ratio ≥0.25, covalent materials have a smaller value (ν = 0.1). The lower and higher boundaries of the central force in solids are 0.25 and 0.5, respectively.[71] Our results indicate that all compounds have ionic contribution and central interatomic forces.

Another crucial factor used to assess the constant nature of the structural qualities in all directions is the anisotropy of materials. A suitable parameter is required to describe the degree of anisotropy, as all single crystals are actually anisotropic. Anisotropy factors for the tetragonal structure are as follows:[44]

$$A_{[100]} = A_1 = A_2 = A = \frac{4C_{44}}{C_{11}+C_{33}-2C_{13}}$$

$$A_{[001]} = A_3 = \frac{4C_{66}}{C_{11}-C_{12}}$$

Table 3 Mulliken atomic population, Mulliken charge (e) and Hirshfeld charge (e) of $Zn_3V_2O_8$, Na_3VO_4 and K_3VO_4

		Mulliken atomic population					
Compounds	Species	s	p	d	Total	Mulliken charge/e	Hirshfeld charge/e
$Zn_3V_2O_8$	Zn	0.34, 0.31	0.65, 0.67	9.97, 9.98	10.97, 10.96	1.03, 1.04	0.46, 0.45
	V	2.25	6.43	3.35	12.03	0.97	0.46
	O	1.86, 1.85	4.73, 4.79, 4.84	0.00	6.59, 6.70, 6.64	−0.59, −0.70, −0.64	−0.28, −0.29
Na_3VO_4	Na	2.14	6.09, 6.10	0.00	8.24	0.76	0.34, 0.32
	V	2.25	6.82	3.42	12.48	0.52	0.49
	O	1.87	4.83	0.00	6.70	−0.70	−0.37
K_3VO_4	K	2.18, 2.11	5.81, 5.96	0.00, 0.00	7.99, 8.07	1.01, 0.93	0.36, 0.45
	V	2.27	6.87	3.44	12.59	0.41	0.45
	O	1.90	4.92	0.00	6.82	−0.82	−0.40

Table 4 Elastic constants C_{ij} (in GPa) of $Zn_3V_2O_8$, Na_3VO_4 and K_3VO_4

Compounds	C_{11}	C_{33}	C_{44}	C_{66}	C_{12}	C_{13}	C_{16}	C_{22}	C_{23}	C_{55}
$Zn_3V_2O_8$	173.98	164.66	53.86	19.44	52.25	87.42	—	182.03	97.04	61.23
Na_3VO_4	71.70	52.97	26.51	20.75	31.70	32.84	0.00	—	—	—
K_3VO_4	50.40	32.07	18.80	11.45	19.19	29.58	0.00	—	—	—

Table 5 Calculated bulk modulus (B), shear modulus (G), Young's modulus (Y), Poisson ratio (ν), Pugh value (G/B), anisotropy factors (A_1, A_2, and A_3), and Kleemann parameter (ξ) of $Zn_3V_2O_8$, Na_3VO_4 and K_3VO_4

Compounds	B_V	B_R	B_H	G_V	G_R	G_H	Y	ν	G/B	A_1	A_2	A_3	ξ
$Zn_3V_2O_8$	110.45	109.5	109.98	45.83	37.3	41.57	110.69	0.33	0.378	1.31	1.60	0.31	0.44
Na_3VO_4	43.46	42.57	43.02	21.35	19.83	20.59	53.26	0.29	2.86	1.79	—	0.14	0.57
K_3VO_4	32.18	31.27	31.72	13.44	7.59	10.52	28.40	0.35	0.33	3.24	—	0.73	0.52

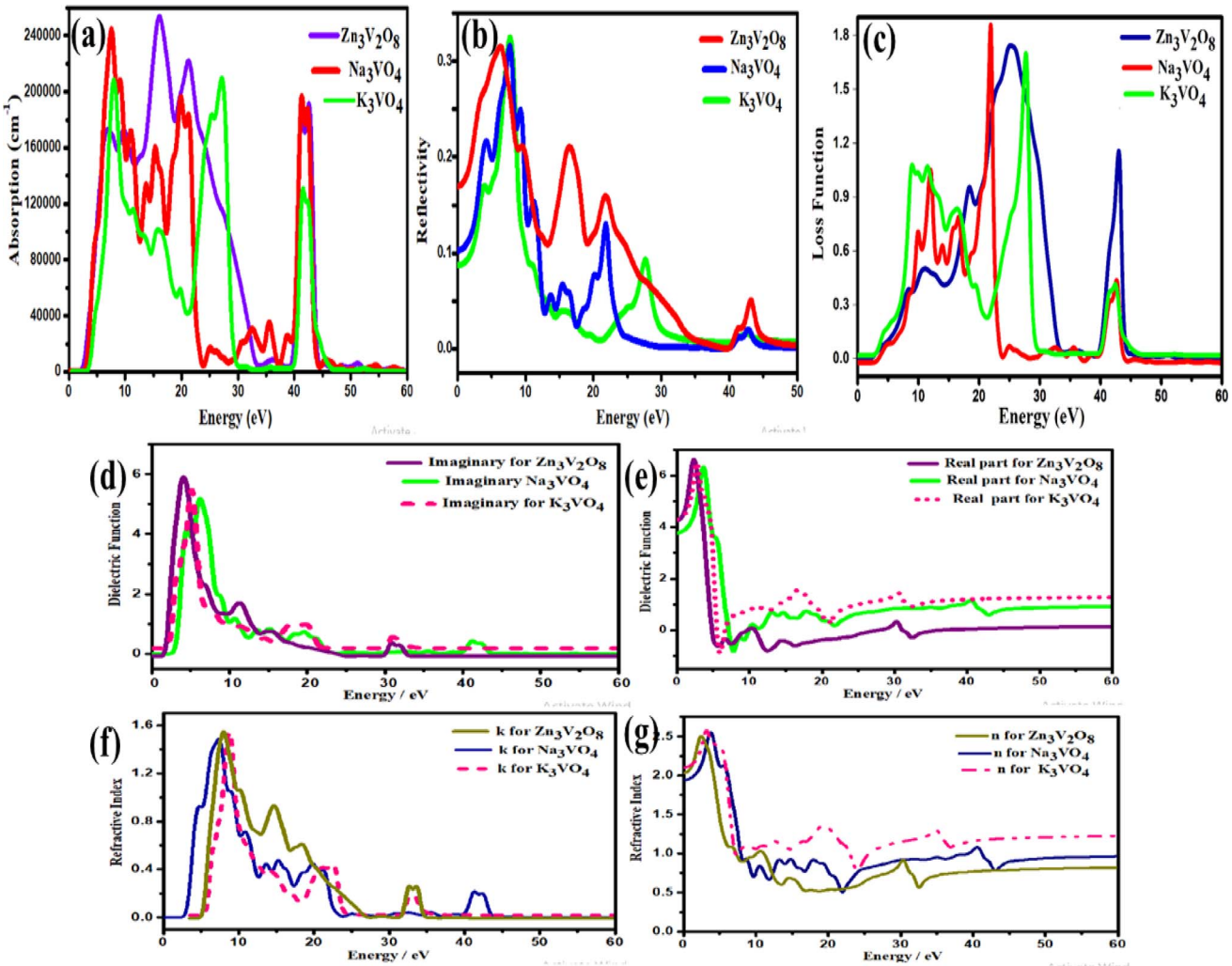

Fig. 15 Optical properties of $Zn_3V_2O_8$, Na_3VO_4 and K_3VO_4: (a) absorption, (b) reflectivity, (c) loss function, (d and e) imaginary & real dielectric function, (f and g) imaginary and real refractive indices.

Using elastic constants, calculations can also be done for the orthorhombic system:

$$A_{[100]} = A_1 = \frac{4C_{44}}{C_{11} + C_{33} - 2C_{13}}$$

$$A_{[010]} = A_2 = \frac{4C_{55}}{C_{22} + C_{33} - 2C_{23}}$$

$$A_{[001]} = A_3 = \frac{4C_{66}}{C_{11} + C_{22} - 2C_{12}}$$

The calculated values of all these parameters are listed in Table 5. As the index for these materials is not zero, all are considered to be anisotropic in nature. Moreover, the elastic anisotropy is associated with the inter-atomic bond strength.

To define the relative positions of the cation and anion sublattices under the maintained volume-strain distortions (for which the positions are variable according to symmetry), Kleemann established a significant factor known as the internal strain parameter (ξ). It describes the coloration of the bond stretching and bending.[44]

$$\xi = \frac{C_{11} + 8C_{12}}{7C_{11} + 2C_{12}}$$

The minimum bond bending is expressed when $\xi = 0$. In the case of $\xi = 1$, there will be minimum bond stretching. Table 5 illustrates that bond-bending is prominent in these photocatalytic materials.

3.8. Optical properties

Optical properties play an important role in determining the photocatalytic activity of photocatalysts, defining their mode of interaction with light. Herein, the absorption, reflection, refractive index, dielectric constant, and loss function are the optical properties calculated in the photon range of 0–60 eV.

3.8.1. Absorption. With electric fields over all directions, the polycrystalline function was used to optimize the optical absorption spectra. A small smearing of 0.5 eV was applied in this simulation to easily detect the absorption peaks. The absorption of incident light by any material can be expressed in terms of the real and imaginary parts of the dielectric function, as described by eqn (1):[40]

$$\alpha(\omega) = \sqrt{2}\,\omega\left[\sqrt{\varepsilon_{\mathrm{Re}}{}^2(\omega) + \varepsilon_{\mathrm{Im}}{}^2(\omega)} - \varepsilon_{\mathrm{Re}}(\omega)\right]^{0.5} \quad (1)$$

The most prominent estimated absorption apexes are 252 269 cm^{-1}, 177 245 cm^{-1}, and 152 260 cm^{-1} for $Zn_3V_2O_8$, Na_3VO_4 and K_3VO_4, respectively. The absorption values fluctuate with increasing photon energy. Meanwhile, optimum values were obtained at about 15.8 eV, 7.39 eV, and 26.9 eV for $Zn_3V_2O_8$, Na_3VO_4 and K_3VO_4, respectively. The absorption cut-off band edge lies at 2.94 eV. This result indicates that the most likely electron transition to occur is VB to CB, as it has been studied for the $BiVO_4$ photocatalyst.[72] All these materials have almost zero absorption in the area of low-frequency photons. The photocatalytic degradation of pollutants is directly related to absorption.[73] Photo-induced charge carriers (electron and hole pairs) are produced when light interacts and activates the photocatalytic material, causing the migration of photosensitive electrons from VB to CB. When these electron and hole pairs interact with water, it results in highly reactive hydroxyl and superoxide radicals. Therefore, these radicals interact with pollutants, and partially or completely degrade them.[14] A lower band gap has a synergetic effect on enhancing the photocatalytic process by allowing the photocatalyst to absorb more photons, and become more sensitive to absorbing incident light.[74] Hence, from Fig. 15a, $Zn_3V_2O_8$ exhibits higher absorption than the other two photocatalyst materials.

3.8.2. Reflectivity. A series of periodic investigations into the optical phenomena initially focused on the reflectivity of the semiconductor material. The reflectivity can also estimate the extent of incident light directed on the surface of a photocatalyst. This estimation correlates with the absorbance character of a material. Earlier studies revealed that a greater UV or visible absorption corresponds to lower reflectivity.[75] Fig. 15b shows a dramatic zigzag pattern in the reflectivity curves. Both Na_3VO_4 and $Zn_3V_2O_8$ have the same reflectance of 0.30 at 6.15 eV and 7.61 eV, respectively. Meanwhile, in the case of K_3VO_4, the optimum $R(\omega)$ is 0.31 at 7.61 eV. The lower reflectivity and higher absorption indicate that $Zn_3V_2O_8$ is a better photocatalytic material.

3.8.3. Loss function. Plasmonic excitations from spectra $L(\omega)$ demonstrate the possible loss of energy per unit length of a transversing electron when light penetrates its surface. Within the validity of dielectric theory, the energy loss function for optical properties is correlated with the dielectric function, as expressed in eqn (2):[76]

$$L(\omega) = \frac{\varepsilon_{\mathrm{Im}}(\omega)}{\varepsilon_{\mathrm{Re}}(\omega) + \varepsilon_{\mathrm{Im}}(\omega)} \quad (2)$$

The high energy region and low energy region are two zones for describing the macroscopic and microscopic parameters of the materials.[6] The critical onset values for the high energy region are 25 eV, 21 eV, and 27 eV for $Zn_3V_2O_8$, Na_3VO_4 and K_3VO_4, respectively. As in the visible region, photocatalysts cannot attenuate incident light, which results in less plasmonic excitation. However, the composition and electronic structure can be designed *via* a low energy function region that is almost less than 1 eV, as shown in Fig. 15c.

3.8.4. Dielectric function. Considering the optical response in the linear range, the complex dielectric function determines all parameters of photocatalyst materials. This function expresses the coupled electron and photon interaction, as given in eqn (3):[76]

$$\varepsilon(\omega) = \varepsilon_{\mathrm{Re}}(\omega) + i\varepsilon_{\mathrm{Im}}(\omega) \quad (3)$$

Here, the frequency of incident light is described by (ω). The real and imaginary parts of the dielectric constants are denoted by $\varepsilon_{Re}(\omega)$ and $i\varepsilon_{\mathrm{Im}}(\omega)$, respectively. The real component defines the electronic polarizability and interaction of incident electromagnetic radiation on materials. The energy storage capability and imaginary number of energy dissipation are also all depicted *via* the real component of this complex function.[77] The maximum real dielectric function is almost the same for all photocatalytic materials (6.31), as shown in Fig. 15e. This optimum value lies at an energy of 3.61 eV. There is a regular variation in the curves with increasing photon energy. After 45 eV of energy, the curve for all materials demonstrates constant behavior.

The initial threshold of the dielectric function's imaginary part is basically referred to as the first absorption peak. Such peaks correlate with the electronic transition between the occupied and unoccupied states near the Fermi level. The electron transition takes place between the V-3d and O-2p states. In addition to some other peaks, the critical onset points for the orthorhombic and tetragonal phases are 5.26 eV and 6.20 eV, respectively. By comparing the function of these three materials, the highest dielectric function of $Zn_3V_2O_8$ confirms its excellent dielectric properties (Fig. 15d).

3.8.5. Refractive index. The refractive index is an important tool for investigating the propagation of incident light

throughout the photocatalytic degradation process. $N(\omega)$ is determined *via* the Kramers–Kronig relationship (eqn (4)):[78]

$$N(\omega) = n(\omega) + ik(\omega) \quad (4)$$

Here, $n(\omega)$ is an absolute refractive index, while $k(\omega)$ is the extinction coefficient. Al Mamum reported that a greater density of the medium is associated with a large value of the refractive index.[6] The refractive index (n) and extinction coefficient (k) are known as "fingerprints of the material" because components of this complex function define the interaction of the material with incident light.[79] $k(\omega)$ represents the attenuation coefficient (imaginary part), which signifies the intensity of dissipated radiation from the material when radiated with incident light. So, the imaginary part of $N(\omega)$ is initiated from zero frequency and increases to a maximum value of 1.38 for Na_3VO_4, 1.52 for $Zn_3V_2O_8$ and K_3VO_4, followed by some fluctuations in curves, as depicted in Fig. 15f.

The variable $n(\omega)$ determines the extent of the electromagnetic wave slowdown in comparison to the vacuum speed. The real part of the complex function of such photocatalyst materials shows an inverse pattern. As depicted in Fig. 15g, $n(\omega)$ has a larger refractive index in the early stage of photon energy than $k(\omega)$, which is virtually zero. Therefore, the real and imaginary parts of the complex $N(\omega)$ function are slightly greater for $Zn_3V_2O_8$ and K_3VO_4, as compared to Na_3VO_4.

3.9. Thermodynamic properties

To analyze the entropy, enthalpy, Gibbs free energy, and specific heat capacity at constant volume, the phonon density of states was calculated (Fig. 16). These parameters have been investigated in temperatures ranging from 0 to 1100 K, where the quasi-harmonic model is valid.[80] Therefore, the phonon contribution to all thermodynamic properties at elevated temperatures is illustrated in this work.

The Gibbs free energy (G) effectively defines the stability of a compound.[81] Fig. 16a shows the variation in the Gibbs free energy of these systems with temperature. The decreasing trend of the Gibbs free energy for the systems is as follows: K_3VO_4 > Na_3VO_4 > $Zn_3V_2O_8$. The Gibbs free energy corresponds to the amount of energy of the system that is required for work to be done. Thus, a system having a lower Gibbs energy (G) is thought to be thermodynamically favorable.[82] The rising trend in the enthalpy and entropy curves with increasing temperature can also be observed in Fig. 16b and c, respectively. The behavior of these two factors is the opposite of that of the Gibbs free energy.[83] Because it possesses the highest entropy, enthalpy,

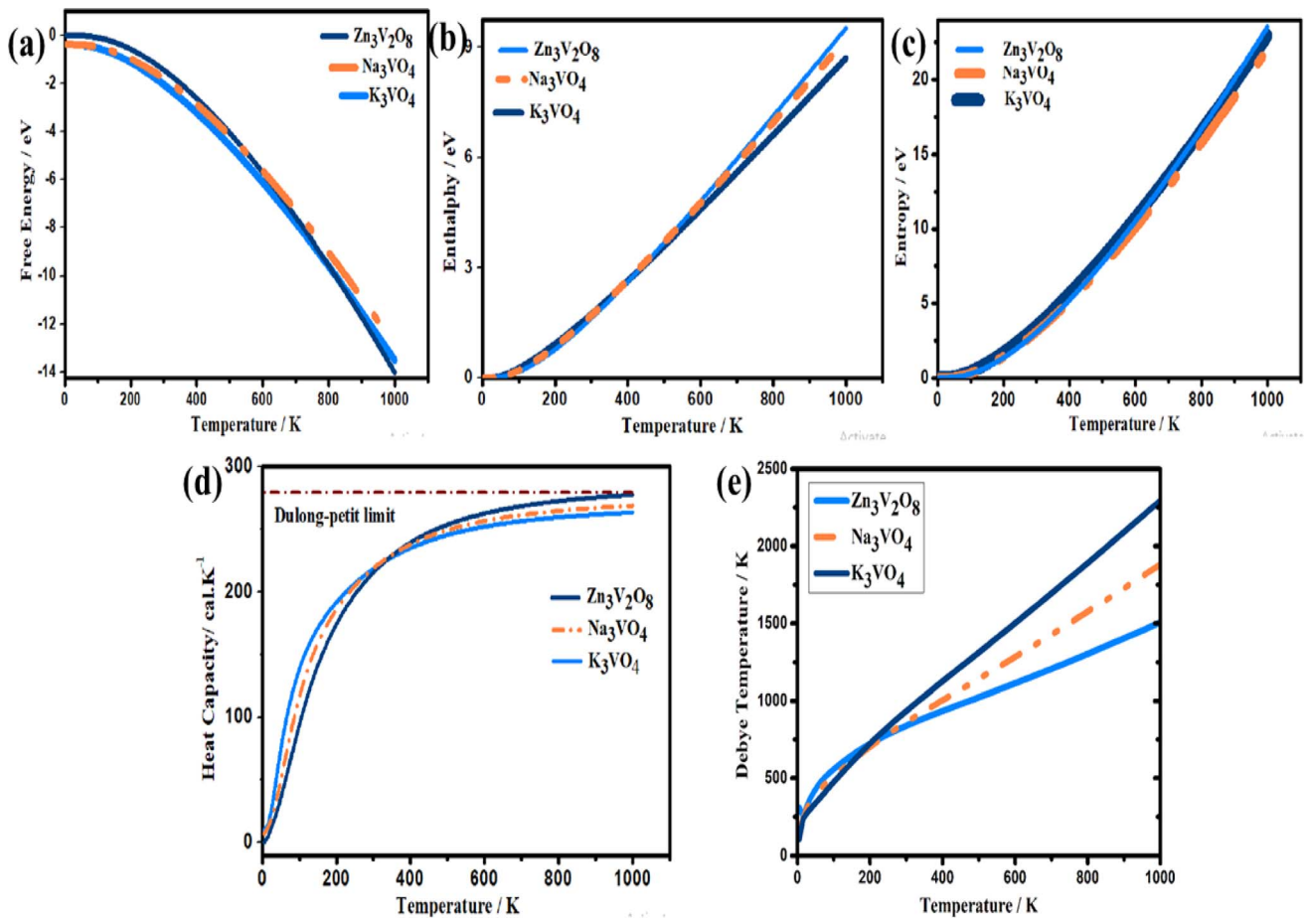

Fig. 16 Calculated thermodynamic parameters, (a) Gibb's free energy, (b) enthalpy, (c) entropy, (d) heat capacity and (e) Debye temperature of Na_3VO_4, K_3VO_4 and $Zn_3V_2O_8$.

and lowest Gibbs energy, the $Zn_3V_2O_8$ photocatalyst is thermodynamically more stable.

Solid-state physics also involves the investigation of a crystal's specific heat capacity at constant volume.[84] The phonon thermal softening at high temperature is highlighted by the increasing trend of the C_v curves. When the temperature is low, C_v is proportional to T^3. However, at elevated temperature, the heat capacity complies with the Dulong–Petit law, and reaches the asymptotic limit, *i.e.*, $3nR$. Here, n is the atom's number in the primitive cell, while R is the general gas constant.[41] The highest heat capacity of $Zn_3V_2O_8$ is 277.29 cal K^{-1} at 1000 K (Fig. 16d).

For qualitative insight into the atomic thermal vibrations, the Debye temperature (θ_D) was studied, as these two parameters are parallel (Fig. 16e). According to the Debye theory, the Debye temperature is compatible with the phonon frequency.[85] Additionally, it represents the stability of the structure and the strength of the bonds, which directly corresponds to several physical characteristics, like the melting temperature and specific heat. The Debye temperature is derived from elastic constants, and observed heat measurements are equivalent at low temperatures. Computing θ_D *via* elastic constants is one of the standard methods of calculation. Thus, the Debye temperature (θ_D) can be estimated from the average sound velocity (ν_m), as described in the following equation:[86]

$$\theta_D = \frac{h}{K_B}\left(\frac{3n}{4\pi V_a}\right)^{\frac{1}{3}}\nu_m$$

Here, h is the Planck's constant. The atomic volume is represented by V_a, and the Boltzmann constant is indicated by K_B. The average sound velocity (ν_m) of a crystalline material can be defined as follows:[44]

$$\nu_m = \left[\frac{1}{3}\left(\frac{1}{\nu_l^3} + \frac{2}{\nu_t^3}\right)\right]^{-\frac{1}{3}}$$

The transverse and longitudinal sound velocities (ν_t and ν_l) of a solid material can be determined from the Navier equation using the values of bulk and shear modulus.

$$\nu_t = \left[\frac{G}{\rho}\right]^{\frac{1}{2}} \text{ and } \nu_l = \left[\left(B + \frac{4}{3}G\right)\frac{1}{\rho}\right]^{\frac{1}{2}}$$

The values of all these parameters are summarized in Table 6. To the best of our knowledge, there is no comparable experimental or theoretical data. Therefore, the stated findings are considered as the first-ever prediction. Thus, these results still need an experimental confirmation.

3.10. Photocatalytic activity

The electronic properties can be used to quantitatively explore the systematic framework of narrowing band gap, separation, and migration of photoinduced charge carriers that will consequently enhance the photoactivity of a substance. However, this improvement might not be enough to achieve the entire photoactivity required for the degradation and water splitting processes.[87] It is obvious that the band structure requires a widely applicable design strategy, including band-edge placements and band gaps of newly produced materials.[88] An efficient tool to examine the enhanced photocatalytic activity of semiconductors for photoelectrochemical water splitting and pollutant degradation is provided by this theoretical calculation method.[89] Inter-particle electron transfer occurs when the optical incident light is equivalent to or greater than the band gap in semiconductor photocatalysts.[90] After the absorption of light, electrons are excited from VB to CB, producing e^- and h^+ charge carriers with oxidative and reductive capabilities.[91] The band edge potentials can be calculated as follows:

$$E_{CB} = \chi - E_e - \frac{1}{2}E_g$$

$$E_{VB} = E_{VB} + E_g$$

Where, the CB and VB edge potentials are denoted by E_{CB} and E_{VB}, respectively, χ is the electronegativity of the semiconductor, and the standard reduction potential (E_e) is estimated as 4.5 eV. The calculated band gap of the photocatalytic material is expressed by E_g. Table 8 and Fig. 17 illustrate the band edge positions of the un-doped and doped $Zn_3V_2O_8$, Na_3VO_4 and K_3VO_4.

The following equation is used to calculate the electronegativity of a material:[87]

$$\chi = \left[\chi^a(\mathrm{R}) \times \chi^b(\mathrm{V}) \times \chi^c(\mathrm{O})\right]^{\frac{1}{(a+b+c)}}$$

Here, a, b, and c represent the number of R (Na, K and Zn), V and O atoms in the compound, respectively. The arithmetic mean of the ionization energy and electron affinity defines the atomic electronegativity of individual atoms ($\chi^a(R) \times \chi^b(V) \times \chi^c(O)$, as discussed in Table 7.

According to the equation, the generation of superoxide acid ($^-HO_2$) and superoxide radical ($O_2^{-\bullet}$) is an essential step for the solar degradation of pollutants. However, photogenerated holes can oxidize the OH^- ion and fabricate the reactive hydroxyl radical (OH^-), as shown in the chemical equations below:[92]

Table 6 Calculated cell volumes, density (ρ), transverse (ν_l) and longitudinal sound velocities (ν_t), average sound velocity and Debye temperature (θ_D) of $Zn_3V_2O_8$, Na_3VO_4 and K_3VO_4

Crystal systems	V (Å^3)	ρ (kg m^{-3})	ν_l (m s^{-1})	ν_t (m s^{-1})	ν_m (ms^{-1})	θ_D
$Zv_3V_2O_8$	600.83	46 500	6446	15 548	7295.71	1520.52
Na_3VO_4	329.38	24 600	2803	5348	3229.71	449.90
K_3VO_4	247.01	26 100	2004	3891	2244.78	344.72

Table 7 First ionization energy (eV), atomic electron affinity (eV) and atomic electronegativity of the individual atoms and dopants

Species	E_{IE} (eV)	E_{EA} (eV)	$\chi = \frac{(E_{IE} + E_{EA})}{2}$
Na	5.13	0.55	2.84
K	4.34	0.50	2.42
Zn	9.39	0	4.70
V	6.74	0.52	3.64
O	13.68	1.46	7.54
Co-dopant	7.88	0.66	4.27
Fe-dopant	7.9	0.16	4.03

Table 8 Calculated electronegativity, band gap (eV), conduction and valence band edge positions (eV) of Na_3VO_4, $Na_3V_{(1-0.06)}Fe_{0.06O4}$, $Na_3V_{(1-0.06)}Co_{0.06}O_4$, K_3VO_4, $K_3V_{(1-0.06)}Fe_{0.06}O_4$, $K_3V_{(1-0.06)}Co_{0.06}O_4$, $Zn_3V_2O_8$, $Zn_{3(1-0.06)}V_{2(1-0.06)}Co_{0.06}O_8$ and $Zn_{3(1-0.06)}V_{2(1-0.06)}Fe_{0.06}O_8$

Compounds	χ	E_g (eV)	CB (eV)	VB (eV)
$Zn_3V_2O_8$	5.80	2.69	−0.63	2.06
$Zn_{3(1-0.06)}V_{2(1-0.06)}Fe_{0.06}O_8$	5.90	1.72	−0.36	1.36
$Zn_{3(1-0.06)}V_{2(1-0.06)}Co_{0.06}O_8$	5.93	1.68	−0.31	1.37
Na_3VO_4	4.77	3.80	−1.63	2.17
$Na_3V_{(1-0.06)}Fe_{0.06O4}$	4.78	2.99	−1.23	1.76
$Na_3V_{(1-0.06)}Co_{0.06O4}$	4.78	2.59	−1.02	1.57
K_3VO_4	4.50	3.65	−1.83	1.82
$K_3V_{(1-0.06)}Fe_{0.06}O_4$	4.50	2.76	−1.38	1.38
$K_3V_{(1-0.06)}Co_{0.06}O_4$	4.53	2.58	−1.26	1.32

$$O_2 + H^+ + e^- \rightarrow HO_2$$

$$O_2 + e^- \rightarrow O_2^{-\bullet}$$

$$OH^- + h^+ \rightarrow OH^{-\bullet}$$

As discussed earlier, the conduction band potential for all of these systems is more negative as compared to the redox potential of $O_2/O_2^{-\bullet}$ (−0.33 eV), indicating the reduction of O_2 to the $O_2^{-\bullet}$ radical anion. Although the conduction band edge potential of the photocatalyst systems is more negative than that of O_2/H_2O_2 (0.685 eV potential), this suggests that H_2O_2 is formed when electrons react with adsorbed oxygen molecules. This H_2O_2 combines with electrons to produce hydroxyl radicals. Furthermore, the valence band potential is more positive than that of $HO^-/HO^\bullet$ potential (1.99 eV), indicating that photogenerated holes in these systems oxidize hydroxyl ions to the reactive hydroxyl radicals required in the photocatalytic degradation of pollutants.[93]

All of the three host systems, either pure, Fe-doped or Co-doped photocatalysts, have a higher positive valence band potential than that of O_2/H_2O (1.23 eV), which is consistent with all of the aforementioned observations, and indicates a strong oxidation potential for the evolution of O_2. Highly reactive radicals ($OH^{-\bullet}$ and $O_2^{-\bullet}$) will oxidize both organic and inorganic substances, resulting in water and other non-toxic molecules.[94] Interestingly, the CB positions of Na_3VO_4, $Na_3V_{0.94}Fe_{0.06}O_4$, $Na_3V_{0.94}Co_{0.06}O_4$, K_3VO_4, $K_3V_{0.94}Fe_{0.06}O_4$, $K_3V0_{.94}Co_{0.06}O_4$, $Zn_3V_2O_8$, $Zn_{2.82}V_{1.88}Fe_{0.12}O_4$, and $Zn_{2.82}V_{1.88}$-$Co_{0.12}O_4$ are negative as compared to the H_2/H^+ (0 eV) redox potential. A more positive potential provides the strong oxidizing potential for oxygen evolution in these photocatalysts, despite the fact that they are efficient at producing hydrogen gas. Higher positive VB and more negative CB potentials are among the best benchmarks for photocatalytic processes.[95] The peculiar higher photocatalytic activity of $Zn_3V_2O_8$ compared to other compounds can be ascribed to the location of the higher V-3d and Fe-3d or Co-3d states, compared with those of Na_3VO_4 and K_3VO_4. For efficient photocatalysis, electron–hole pairs should be energetically and geometrically separated.

Solubility is a key parameter in determining the photocatalytic efficiency. At present, most of the photocatalytic materials usually comprised insoluble semiconductors, while soluble semiconductor materials have restricted validity in photocatalysis.[96] Soluble inorganics can dissolve in water due to the attraction of positive and negative charges, resulting in the disintegration of crystalline structures and the loss of energy

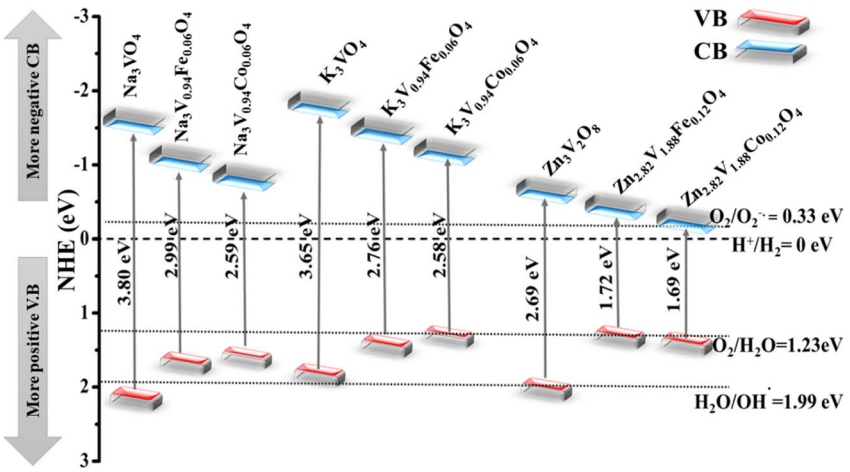

Fig. 17 Schematic with band edge positions of pure and doped Na_3VO_4, K_3VO_4, and $Zn_3V_2O_8$ in the photocatalytic water splitting process.

band structures for light absorption.[97] Meanwhile, the addition of an insoluble solute to its saturated solution will remain as crystals, and these undissolved photocatalytic materials will retain the geometrical shapes required for light absorption and photogenerated carrier transfer.[96] Higher lattice energies are typically associated with less solubility because they demand more energy to break the ionic bonds within the lattice.[98] Lattice energy minimization techniques have been used in attempt to enhance the effectiveness of water-soluble photocatalysts.[99] The lattice energy of $Zn_3V_2O_8$ (−50340.43 eV) is highest among all three studied orthovanadates, indicating its lowest solubility as compared to K_3VO_4 and Na_3VO_4 (Table 1). Moreover, the smaller size and greater charge on the Zn^{2+} ion than Na^+ and K^+ ions enables it to develop the strongest forces of attraction within the lattice, which are difficult to overcome, hence making it significantly less soluble in water. Furthermore, neither distortion of the crystal lattice nor significant reduction in the lattice energy was observed after doping. The solubility trend for all un-doped and doped orthovanadates is as follows: $Zn_3V_2O_8$ > $Zn_{3(1-0.06)}V_{2(1-0.06)}Co_{0.06}O_8$ > $Zn_{3(1-0.06)}V_{2(1-0.06)}$-$Fe_{0.06}O_8$ > Na_3VO_4 > $Na_3V_{(1-0.06)}Co_{0.06}O_4$ > $Na_3V_{(1-0.06)}Fe_{0.06}O_4$ > K_3VO_4 > $K_3V_{(1-0.06)}Co_{0.06}O_4$ > $K_3V_{(1-0.06)}Fe_{0.06}O_4$.

4. Conclusion

This study explored the first-principles calculations of vanadium-based Na_3VO_4, K_3VO_4, and $Zn_3V_2O_8$ photocatalysts. The covalent character is associated with a higher degree of positive charge (for the V–O and R–O bonds). Moreover, the shorter bond length and high electronegativity of the V–O bond introduce hardness in all of these materials. The elastic constants and aggregate elastic modulus (*B*, *G*, *Y*, G/B, Poisson ratio) are also discussed, which signify the stiffness, ductility, anisotropy, and mechanical stability of these compounds. Using a quasi-harmonic approach, the thermodynamic parameters illustrated that a sharp decline in the Gibbs energy can be observed with increased temperature. The increasing heat capacity approaches the Dulong–Petit limit. Hence, K_3VO_4, Na_3VO_4, and $Zn_3V_2O_8$ are thermodynamically stable photocatalysts. As optical properties, materials showing lower reflectivity and higher absorption are associated with a high dielectric constant, so these parameters actually enhance the photocatalytic activity. A more negative CB value and a more positive VB value are appropriate criteria for photocatalytic water splitting and pollutant degradation. Na_3VO_4 is photocatalytically more active despite its prominent flaw, *i.e.*, band gap, which can be resolved in the future. The electronic structure of a narrow band gap is significantly influenced by cations without a noble gas configuration. The estimated indirect band gap of $Zn_3V_2O_8$ is 2.69 eV, which is less than the values of 3.80 eV and 3.65 eV for Na_3VO_4 and K_3VO_4, respectively. However, doping with 6% iron and 6% cobalt turned the indirect band gap into a direct one with a prominent reduction in the band gap, especially with 6% Co as compared to 6% Fe. When the electronegativity of the doping species is smaller than that of oxygen, the impurity states will lie above the V. B. M. As a result, interactions between Co 3d and O 2p, as demonstrated by PDOS and the spin up (α) and spin down (β) magnetic moments, destabilize the VB and dramatically reduce the band gap, leading to the most effective photoresponse of $Zn_{3(1-0.06)}V_{2(1-0.06)}Co_{0.06}O_8$ under visible light irradiation. Furthermore, based on the definition of the semiconductor electronegativity, the CB and VB edge positions demonstrated that the Fe or Co-doped $Zn_3V_2O_8$ possesses favorable redox potentials under visible light, making it a promising material for further applications.

Data availability

All data are present in the manuscript.

Conflicts of interest

There are no conflicts to declare.

References

1 V. Dhiman and N. Kondal, *Phys. B*, 2022, **628**, 413569.
2 M.-Y. Qi, M. Conte, M. Anpo, Z.-R. Tang and Y.-J. Xu, *Chem. Rev.*, 2021, **121**, 13051–13085.
3 K. Nakata and A. Fujishima, *J. Photochem. Photobiol., C*, 2012, **13**, 169–189.
4 E. M. Saggioro, A. S. Oliveira and J. C. Moreira, *Text Wastewater Treat*, 2016.
5 Z. Shayegan, C.-S. Lee and F. Haghighat, *Chem. Eng. J.*, 2018, **334**, 2408–2439.
6 A. Al Mamun, M. Monsur Alam, A. Habib, U. Chakma, M. Sikder and A. Kumer, *Egypt. J. Chem.*, 2021, **64**, 5117–5126.
7 C. Karthikeyan, P. Arunachalam, K. Ramachandran, A. M. Al-Mayouf and S. Karuppuchamy, *J. Alloys Compd.*, 2020, **828**, 154281.
8 Y. Chen, C. Shen, J. Wang, G. Xiao and G. Luo, *ACS Sustain. Chem. Eng.*, 2018, **6**, 13276–13286.
9 R. A. Omar, D. Chauhan, N. Talreja, R. Mangalaraja and M. Ashfaq, in *Agri-Waste and Microbes for Production of Sustainable Nanomaterials*, Elsevier, 2022, pp. 281–298.
10 S. Tu, Y. Guo, Y. Zhang, C. Hu, T. Zhang, T. Ma and H. Huang, *Adv. Funct. Mater.*, 2020, **30**, 2005158.
11 K. W. Bourkeb and O. Baaloudj, *J. Solid State Electrochem.*, 2022, **26**, 571–580.
12 C. Hitam and A. Jalil, *J. Environ. Manage.*, 2020, **258**, 110050.
13 C. V. Reddy, I. N. Reddy, K. Ravindranadh, K. R. Reddy, D. Kim and J. Shim, *Sep. Purif. Technol.*, 2020, **252**, 117352.
14 K. M. Lee, C. W. Lai, K. S. Ngai and J. C. Juan, *Water Res.*, 2016, **88**, 428–448.
15 K. Prakash, P. Senthil Kumar, S. Pandiaraj, K. Saravanakumar and S. Karuthapandian, *J. Exp. Nanosci.*, 2016, **11**, 1138–1155.
16 Q. Guo, C. Zhou, Z. Ma and X. Yang, *Adv. Mater.*, 2019, **31**, 1901997.
17 Y. Dai, C. Poidevin, C. Ochoa-Hernández, A. A. Auer and H. Tüysüz, *Angew. Chem.*, 2020, **132**, 5837–5845.
18 X. Liu, S. Depaifve, T. Leyssens, S. Hermans and A. Vlad, *Batteries Supercaps*, 2019, **2**, 1016–1025.

19 M. R. Dolgos, A. M. Paraskos, M. W. Stoltzfus, S. C. Yarnell and P. M. Woodward, *J. Solid State Chem.*, 2009, **182**, 1964–1971.
20 W. Zhang, H. Zhang, W. Huang, X. Lu, S. Gao, J. Wang, D. Zhang, X. Zhang and M. Wang, *Inorg. Chem. Front.*, 2022, **9**, 977–986.
21 T. Iqbal, A. Hassan, M. Ijaz, M. Salim, M. Farooq, M. Zafar and M. Tahir, *Appl. Nanosci.*, 2021, **11**, 1661–1671.
22 T. Nakajima, M. Isobe, Y. Uzawa and T. Tsuchiya, *J. Mater. Chem. C*, 2015, **3**, 10748–10754.
23 C.-M. Huang, G.-T. Pan, Y.-C. M. Li, M.-H. Li and T. C.-K. Yang, *Appl. Catal., A*, 2009, **358**, 164–172.
24 R. Mohamed, F. Harraz and I. Mkhalid, *J. Alloys Compd.*, 2012, **532**, 55–60.
25 J. Ye, Z. Zou, M. Oshikiri, A. Matsushita, M. Shimoda, M. Imai and T. Shishido, *Chem. Phys. Lett.*, 2002, **356**, 221–226.
26 A. Malathi, J. Madhavan, M. Ashokkumar and P. Arunachalam, *Appl. Catal., A*, 2018, **555**, 47–74.
27 M. M. Sajid, N. A. Shad, S. B. Khan, Z. Zhang and N. Amin, *J. Alloys Compd.*, 2019, **775**, 281–289.
28 B. Slobodin, A. Ishchenko, R. Samigullina, O. Teslenko, B. Shul'gin and D. Y. Zhurakovskii, *Inorg. Mater.*, 2011, **47**, 1126–1131.
29 F. Wang, T. Shen, Z. Fu, Y. Lu and C. Chen, *Nanotechnology*, 2017, **29**, 035702.
30 İ. Tatlıdil, E. Bacaksız, C. K. Buruk, C. Breen and M. Sökmen, *J. Alloys Compd.*, 2012, **517**, 80–86.
31 A. James, J. D. Rodney, A. Manojbabu, S. Joshi, L. Rao, B. R. Bhat and N. Udayashankar, *J. Mater. Sci.: Mater. Electron.*, 2024, **35**, 190.
32 C. Ponraj, P. S. Kumar, S. Sarkar, C. Krishnamoorthi, N. Manikandan, G. Vinitha and J. Daniel, *Surf. Interfaces*, 2022, **31**, 102050.
33 M. A. Khan, S. I. Woo and O.-B. Yang, *Int. J. Hydrogen Energy*, 2008, **33**, 5345–5351.
34 S. Piskunov, O. Lisovski, J. Begens, D. Bocharov, Y. F. Zhukovskii, M. Wessel and E. Spohr, *J. Phys. Chem. C*, 2015, **119**, 18686–18696.
35 C. Regmi, Y. K. Kshetri, T.-H. Kim, R. P. Pandey and S. W. Lee, *Mol. Catal.*, 2017, **432**, 220–231.
36 M. Segall, P. J. Lindan, M. a. Probert, C. J. Pickard, P. J. Hasnip, S. Clark and M. Payne, *J. Phys.: Condens. Matter*, 2002, **14**, 2717.
37 S. Hall, I. Hamerton, B. Howlin and A. Mitchell, *Mol. Simul.*, 2008, **34**, 1259–1266.
38 S. Fagan, R. Mota, R. J. Baierle, G. Paiva, A. Da Silva and A. Fazzio, *J. Mol. Struct.: THEOCHEM*, 2001, **539**, 101–106.
39 J. P. Perdew, K. Burke and M. Ernzerhof, *Phys. Rev. Lett.*, 1996, **77**, 3865.
40 M. Neumann and O. Steinhauser, *Chem. Phys. Lett.*, 1983, **102**, 508–513.
41 X. Jin, R. Wang, Y. Zhou, J. Lai, J. Li, G. Pei, S. Chen, X. Wang, J. Xiang and Z. Zhu, *J. Alloys Compd.*, 2022, **896**, 162862.
42 A. B. Garg, D. Errandonea, P. Rodríguez-Hernández and A. Muñoz, *J. Phys.: Condens. Matter*, 2016, **29**, 055401.
43 S. Tang, C. Zhang, C. Jia, H. Ryu, C. Hwang, M. Hashimoto, D. Lu, Z. Liu, T. P. Devereaux and Z.-X. Shen, *APL Mater.*, 2018, **6**, 026601.
44 A. F. U. Islam, M. N. H. Liton, H. T. Islam, M. Al Helal and M. Kamruzzaman, *Chin. Phys. B*, 2017, **26**, 036301.
45 S.-F. Sheng, *Phys. B*, 2013, **426**, 20–23.
46 Z. Huang, L. Zhang and W. Pan, *J. Solid State Chem.*, 2013, **205**, 97–103.
47 J. Zhang, P. Zhou, J. Liu and J. Yu, *Phys. Chem. Chem. Phys.*, 2014, **16**, 20382–20386.
48 R. Wallauer, R. Perea-Causin, L. Münster, S. Zajusch, S. Brem, J. Güdde, K. Tanimura, K.-Q. Lin, R. Huber and E. Malic, *Nano Lett.*, 2021, **21**, 5867–5873.
49 R. Liu, Z. Chen, Y. Yao, Y. Li, W. A. Cheema, D. Wang and S. Zhu, *RSC adv.*, 2020, **10**, 29408–29418.
50 Z. Luo, X. Chen, J. Chen and X. Wang, *Eur. J. Oper. Res.*, 2017, **259**(2), 437–451.
51 R. Gedam and D. Ramteke, *J. Rare Earths*, 2012, **30**, 785–789.
52 A. Chaudhuri, L. Mandal, X. Chi, M. Yang, M. Scott, M. Motapothula, X. Yu, P. Yang, Y. Shao-Horn and T. Venkatesan, *Phys. Rev. B*, 2018, **97**, 195150.
53 S. S. Kekade, P. V. Gaikwad, S. A. Raut, R. J. Choudhary, V. L. Mathe, D. Phase, A. Kshirsagar and S. I. Patil, *ACS Omega*, 2018, **3**, 5853–5864.
54 A. Langenberg, K. Hirsch, A. Ławicki, V. Zamudio-Bayer, M. Niemeyer, P. Chmiela, B. Langbehn, A. Terasaki, B. v. Issendorff and J. Lau, *Phys. Rev. B*, 2014, **90**, 184420.
55 M.-H. Lv, C.-M. Li and W.-F. Sun, *Nanomaterials*, 2022, **12**, 382.
56 M. Zhang, Z. Huang, X. Wang, H. Zhang, T. Li, Z. Wu, Y. Luo and W. Cao, *Sci. Rep.*, 2016, **6**, 19504.
57 J. Zhang, D. Gao and K. Xu, *Sci. China: Phys., Mech. Astron.*, 2012, **55**, 428–435.
58 V. K. Sharma and G. D. Varma, *Adv. Mater. Lett.*, 2012, **3**, 126–129.
59 L. Ren, J. Xu, S.-C. Pan, H.-Y. Yu, T. Zhang, T. Shoji, N.-N. Li, D.-Y. Zhang and D.-B. Sun, *Colloids Surf., A*, 2021, **617**, 126393.
60 J.-H. Wang and Z.-Y. Zhao, *Materials*, 2022, **15**, 1361.
61 A. Mirzai, S. Melin and A. Ahadi, *Comput. Mater. Sci.*, 2022, **214**, 111741.
62 F. Subhan, S. Azam, G. Khan, M. Irfan, S. Muhammad, A. G. Al-Sehemi, S. Naqib, R. Khenata, S. Khan and I. V. Kityk, *J. Alloys Compd.*, 2019, **785**, 232–239.
63 F. Mouhat and F.-X. Coudert, *Phys. Rev. B*, 2014, **90**, 224104.
64 L. Zuo, M. Humbert and C. Esling, *J. Appl. Crystallogr.*, 1992, **25**, 751–755.
65 Z. Huang, J. Feng and W. Pan, *J. Solid State Chem.*, 2012, **185**, 42–48.
66 C. Chen, L. Liu, Y. Wen, Y. Jiang and L. Chen, *Crystals*, 2019, **9**, 497.
67 V. Kumar, A. Shrivastava and V. Jha, *J. Phys. Chem. Solids*, 2010, **71**, 1513–1520.
68 K. Panda and K. R. Chandran, *Acta Mater.*, 2006, **54**, 1641–1657.
69 M. Ali, M. Hadi, M. Hossain, S. Naqib and A. Islam, *Phys. Status Solidi B Basic Res.*, 2017, **254**, 1700010.

70 M. A. Rahman, M. Z. Rahaman and M. A. Rahman, *Int. J. Mod. Phys. B*, 2016, **30**, 1650199.
71 M. J. Islam, M. S. H. Sohag, U. Chakma, A. Kumer, M. M. Alam and M. Nazrul Islam Khan, *Advances in Condensed Matter Physics*, 2023, p. 2023.
72 J. Liu, F. Liu, H. Bai, W. Zhuang and Y. Xu, *Mol. Phys.*, 2022, **120**, e2002958.
73 S. Pasternak and Y. Paz, *ChemPhysChem*, 2013, **14**, 2059–2070.
74 N. Khalid, A. Hammad, M. Tahir, M. Rafique, T. Iqbal, G. Nabi and M. Hussain, *Ceram. Int.*, 2019, **45**, 21430–21435.
75 M. J. Islam and A. Kumer, *SN Appl. Sci.*, 2020, **2**, 251.
76 M. Houari, B. Bouadjemi, M. Matougui, S. Haid, T. Lantri, Z. Aziz, S. Bentata and B. Bouhafs, *Opt. Quantum Electron.*, 2019, **51**, 1–14.
77 B. Zhao, Y. Du, Z. Yan, L. Rao, G. Chen, M. Yuan, L. Yang, J. Zhang and R. Che, *Adv. Funct. Mater.*, 2023, **33**, 2209924.
78 M. A. Kamboh, L. Hao, M. Farhan, Y. Su, L. Wang, Q. Chen, H. Wang, J. Zhang and Q. Wang, *J. Mater. Sci.*, 2022, **57**, 18905–18922.
79 S. Kanwal, J. Wen, B. Yu, X. Chen, D. Kumar, Y. Kang, C. Bai, S. Ubaid and D. Zhang, *Nanomaterials*, 2020, **10**, 1439.
80 M. Isik, G. Surucu, A. Gencer and N. Gasanly, *Mater. Today Commun.*, 2021, **27**, 102299.
81 J. Buckeridge, D. O. Scanlon, A. Walsh and C. R. A. Catlow, *Comput. Phys. Commun.*, 2014, **185**, 330–338.
82 B. H. Solis and S. Hammes-Schiffer, *Inorg. Chem.*, 2014, **53**, 6427–6443.
83 S. J. McCormack and A. Navrotsky, *Acta Mater.*, 2021, **202**, 1–21.
84 L. Qiu, N. Zhu, Y. Feng, E. E. Michaelides, G. Żyła, D. Jing, X. Zhang, P. M. Norris, C. N. Markides and O. Mahian, *Phys. Rep.*, 2020, **843**, 1–81.
85 G. J. Snyder, M. T. Agne and R. Gurunathan, *Natl. Sci. Rev.*, 2019, **6**, 380–381.
86 S. Boucetta and F. Zegrar, *J. Magnesium Alloys*, 2013, **1**, 128–133.
87 D. Toprek and V. Koteski, *Mater. Chem. Phys.*, 2021, **264**, 124439.
88 B.-X. Zhou, W.-Q. Huang, K. Yang, S. S. Ding, Z. Xie, A. Pan, W. Hu, P. Peng and G.-F. Huang, *J. Phys. Chem. C*, 2018, **122**, 28065–28074.
89 R. Saravanan, S. Karthikeyan, V. Gupta, G. Sekaran, V. Narayanan and A. Stephen, *Mater. Sci. Eng. C*, 2013, **33**, 91–98.
90 D. Zheng and X. Wang, *Appl. Catal., B*, 2015, **179**, 479–488.
91 P. Praus, *Carbon*, 2021, **172**, 729–732.
92 H. Yan, X. Wang, M. Yao and X. Yao, *Prog. Nat. Sci.: Mater. Int.*, 2013, **23**, 402–407.
93 F. Opoku, K. K. Govender, C. G. C. E. van Sittert and P. P. Govender, *New J. Chem.*, 2017, **41**, 11701–11713.
94 C. Bie, H. Yu, B. Cheng, W. Ho, J. Fan and J. Yu, *Adv. Mater.*, 2021, **33**, 2003521.
95 I. Székely, E.-Z. Kedves, Z. Pap and M. Baia, *Catalysts*, 2021, **11**, 779.
96 W. Gao, Y. Wang, M. Zhong, H. Kang, B. Su and Z. Lei, *Colloids Surf., A*, 2024, 135110.
97 G. Iervolino, I. Zammit, V. Vaiano and L. Rizzo, *Heterogeneous Photocatalysis: Recent Advances*, 2020, 225–264.
98 P. Reunchan, S. Ouyang, N. Umezawa, H. Xu, Y. Zhang and J. Ye, *J. Mater. Chem. A*, 2013, **1**, 4221–4227.
99 C. Parks, A. Koswara, F. DeVilbiss, H.-H. Tung, N. K. Nere, S. Bordawekar, Z. K. Nagy and D. Ramkrishna, *Phys. Chem. Chem. Phys.*, 2017, **19**, 5285–5295.